IMPLEMENTATION OF PASSIVE AND ACTIVE MATERIAL BEHAVIOUR OF CARDIAC TISSUE INTO THE FINITE ELEMENT SOFTWARE ABAQUS VIA A USER SUBROUTINE

A thesis submitted to the Delft University of Technology in partial fulfillment
of the requirements for the degree of

Master of Science in Biomedical Engineering

by

Anna Kuiken

June 2022

ABSTRACT

Intro - The rapidly developing technology of cardiac finite element modelling aims to improve heart failure treatment by quantifying stresses acting in the cardiac tissue. Cardiac finite element modelling may improve heart failure treatment by providing more insight in the pathophysiology, enabling a patient-specific assessment and improving the efficiency of clinical trials and medical devices. An essential part of the cardiac finite element model is capturing the mechanical behaviour of the heart, including its active behaviour (contraction). This mechanical behaviour is captured by means of a material model. However, the active behaviour of the heart is not readily available in material models provided by commercial finite element software like Abaqus/CAE. Consequently, such active material model needs to be added in a user subroutine manually. This is a time-consuming task, prone to errors. Additionally, the availability of the documentation is limited, and in literature the methodology of the implementation is oftentimes not disclosed.

Thesis goal - The goal of this master-thesis is to implement a combination of the passive and active mathematical material models in a commercial finite element platform. This was done by implementing the combined material models in user subroutine UMAT that can be used in FEA-software Abaqus. Reproducibility of the UMAT is ensured by a detailed documentation. Also, the UMAT is provided in the supplementary material.

Methods - The UMAT consists of the Holzapfel Ogden constitutive law as passive component, and the Time Varying-Elastance contstitutive law as active component, which are combined by means of the active stress approach. Additionally, the UMAT requires computation of the elasticity tensor, which is computed by means of a numerical formulation. The incorporation of the passive and active constitutive laws in the UMAT was verified by means of multiple test-cases. The outcomes of the UMAT were compared to an analytical solution and a benchmark user subroutine in the form of UANISOHYPER_INV. Lastly, reality-check test-cases were carried out by comparing the UMAT outcomes to the results from similar test-cases found in literature.

Verification results - Verification of the implemented material models showed good agreement with the analytical computed solution of equibiaxial extension, equibiaxial compression and isometric contraction test-cases, as all cases showed an MAPE_{max} or APE_{max} error lower than 1%. Shear test-case results of the UMAT showed some bigger APE_{max} values (maximal 17%) with relation to the analytical solution, possibly caused by numerical errors during the elasticity tensor computation. Results of the reality-check cases showed similar trends to the mechanical experiments done on cardiac tissue on which these cases are based.

Conclusion - The public availability of the implemented passive and active material models in the user subroutine UMAT, which is working reasonably well according to conducted verification, forms a significant step forwards in the field of cardiac finite element modelling. The current work can be further extended by the incorporations of compressibility during contraction and viscoelasticity in the material models. This thesis provides the basis for future projects in the field of cardiac finite element modelling including an active material model. Also, the provided implementation of material models may aid in the implementation of other mathematical material models in a user subroutine like UMAT.

CONTENTS

ABBREVIATIONS

CONVENTIONS

Lowercase greek lettres are used for scalars, lowercase bold-face Latin letters are used for vectors, uppercase bold-face Latin letters are used for second-order tensors (or matrices), double Latin letters are used for fourth-order tensors. E.g.:

$\mathbf{a}, \mathbf{b}, \mathbf{c}$,...(1st-order tensors or vectors)

$\mathbf{A}, \mathbf{B}, \mathbf{C}$,...(2nd-order tensors or matrices)

$\mathbb{A}, \mathbb{B}, \mathbb{C}, \mathbb{a}, \mathbb{b}, \mathbb{c}$,...(4th-order tensors)

Basic Continuum Mechanics

$\mathbf{x}_0$ and $\mathbf{x}$ are vectors related to material points of an undeformed (reference) and deformed (current) form configuration of a continuum body, respectively.

$$\mathbf{F} = \frac{\partial \mathbf{x}}{\partial \mathbf{x}_0} \qquad = \text{deformation gradient}$$

$$J = det(\mathbf{F}) \qquad = \text{determinant}$$

$$\overline{\mathbf{F}} = J^{-1/3}\mathbf{F} \qquad = \text{isovolumetric part of the deformation gradient}$$

$$\mathbf{C} = \mathbf{F}^T\mathbf{F} \qquad = \text{right Cauchy-Green deformation tensor}$$

$$\overline{\mathbf{C}} = \overline{\mathbf{F}}^T\overline{\mathbf{F}} \qquad = \text{isovolumetric part of } \mathbf{C}$$

$$\mathbf{B} = \mathbf{F}\mathbf{F}^T \qquad = \text{left Cauchy-Green deformation tensor}$$

$$\overline{\mathbf{B}} = \overline{\mathbf{F}}\overline{\mathbf{F}}^T \qquad = \text{isovolumetric part of } \mathbf{B}$$

$$E^G = \frac{1}{2}(\mathbf{C} - \mathbf{I}) \qquad = \text{Green-Lagrangian strain tensor (2nd order tensor)}$$

$$E^N = \sqrt{\mathbf{C}} - \mathbf{I} \qquad = \text{Nominal or Engineering strain tensor (2nd order tensor)}$$

$$\delta_{ij} = \begin{cases} 1 & \text{if } i = j \\ 0 & \text{if } i \neq j \end{cases} \qquad = \text{the kronecker delta}$$

Table 0.1: Symbols used in this thesis

Symbol	Meaning
Deformation Gradients	
$\mathbf{F^{EE}}$	Deformation gradient defined in a global coordinate system.
$\mathbf{F^{eE}}$	Deformation gradient defined in a co-rotational local coordinate system.
$\mathbf{F}^{al}$	Deformation gradient form that is given to the UMAT by Abaqus when a local fibre direction is defined with the keyword *Orientation.
$\mathbf{U}$	The stretch matrix.
$\mathbf{R}$	The rotation matrix.
J	The determinant of $\mathbf{F}$.
Strain Energy Function	
Ψ	The (Holzapfel and Ogden (HO)) strain energy function.
a_i, b_i	Material parameters, with $i = 1, 4f, 4s$ and $8fs$.
$\bar{I}_i$	Invariants of the strain energy function (SEF) with $i = 1, 4f, 4s$ and $8fs$.
ψ_i	The first derivative of Ψ w.r.t. invariants $\bar{I}_i$, with $i = 1, 4f, 4s$ and $8fs$.
ψ_i''	The second derivative of Ψ w.r.t. invariants $\bar{I}_i$, with $i = 1, 4f, 4s$ and $8fs$.
$\mathbf{f}_0, \mathbf{s}_0$	Vectors denoting the fibre and sheet orientation in reference configuration.
$\mathbf{f}, \mathbf{s}$	Vectors denoting the fibre and sheet orientation in deformed configuration.
κ	The bulk modulus.
Stress Measures	
$\mathbf{S}$	The 2nd Piola-Kirchhoff stress.
$\bar{\mathbf{S}}$	The fictitious 2nd Piola-Kirchhoff stress.
τ	Kirchhoff stress.
σ	Cauchy stress.
$\sigma_{pas/act}$	Passive and active part of the cauchy stress.
$\sigma_{iso/vol}$	Isovolumetric and volumetric part of the (passive) cauchy stress.
$\sigma_{af/as}$	Active cauchy stress in fibre or sheet direction.
n	A scaling value.
$\bar{\sigma}$	The fictitious cauchy stress.
p	Penalty parameter.
$\chi_*(\bullet)$	Push forward operation.
Tangent Matrix	
$\mathbb{C}$	Material form of the elasticity tensor.
$\mathbb{c}$	Spatial form of the elasticity tensor.
$\overline{\mathbb{C}}$	Fictitious material form of the elasticity tensor.
$\overline{\mathbb{c}}$	Fictitious spatial form of the elasticity tensor.
$\tilde{p}$	Scalar function of $\mathbb{C}$.
$\mathbb{P}$	Fourth order projection tensor in reference configuration.
$\mathbb{I}$	Fourth order unit tensor.
Jaumann Rate	
$\tilde{\mathbb{c}}^{\tau}$	Jaumann rate (dependent on τ).
$\tilde{\mathbb{c}}^{\sigma}$	Jaumann rate (dependent on σ).
Perturbation Method	
$\hat{\mathbf{F}}^{(ij)}$	Perturbed deformation gradient in only its (i,j) component.
$J_p^{(ij)}$	The determinant of the perturbed deformation gradient in only its (i,j) component.
θ	A small perturbation parameter.

1 INTRODUCTION: MODELLING OF CARDIAC TISSUE

1.1 THESIS GOAL

Heart failure is a life-threatening disease, causing decrease in functionality, quality of life and mortality, affecting more than 64 million people globally [1]. Heart failure is a syndrome characterised by decreased cardiac output caused by a structural and/or functional cardiac abnormality [1]. Next to its medical burden, it also causes socioeconomic burden, with a cost estimation of $30.7 billion dollar in the USA in 2012. Costs are predicted to increase further to $69.8 billion dollars in 2030 [2].

A rapidly developing technology aiming to improve treatment of heart failure by quantifying stresses acting in the cardiac tissue, are cardiac finite element (FE) models. Stress quantification by means of cardiac FE models may enable a more patient-specific medical treatment, as they include the anatomy and physiology of the individual patient in the treatment decision (e.g. [3], [4]). Also, cardiac FE models may improve the efficiency of clinical trials of medical devices (e.g. [4], [5]). Lastly, more insight in the pathophysiology of cardiac diseases may be obtained by the development of cardiac FE models.

An essential part of the cardiac FE model is the material model, as it describes the stress-strain behaviour of the cardiac tissue. Ideally, the material model that is implemented in a whole heart model, characterises both the passive component and the active component (the cardiac contraction) of the cardiac tissue. Although multiple pre-programmed material models exist that are compatible with biological tissues (e.g. the Holzapfel-Gasser-Ogden model), material models that enable contraction of the material are not readily available in commercial FE software like Abaqus/CAE [6]. Consequently, for such applications biomedical engineers turn to programming existing passive and active mathematical material models (constitutive laws) into a user subroutine themselves. This is a time-consuming task, prone to errors [7], of which limited documentation is available. Additionally, in literature the methodology of the implementation is oftentimes omitted.

The goal of this master-thesis is to provide a detailed report and implementation of two combined mathematical material models in a commercial FE platform, widely used by the computational biomechanics community. This was done by implementing the combined material models in the user subroutine UMAT that can be used in FEA-software Abaqus. The development of this specific user subroutine is documented in detail and provided in the supplementary material to enable reproduction. Secondly, it can aid during the implementation of other mathematical material models in a user subroutine.

The UMAT consists of the Holzapfel and Ogden (HO) constitutive law as passive component [8], and the time-varying elastance (TVE) model as active component [9], which are combined by means of the active stress approach. The elasticity tensor is implemented by means of a numerical formulation. Subsequently to the implementation, the active and passive components were thoroughly verified by means of multiple test-cases, which compared the outcomes of the user subroutine to an analytical solution and a benchmark user subroutine in the form of UANISOHYPER_INV. Lastly, reality-check test-cases were carried out, comparing the outcomes of the model to similar mechanical tests done in literature.

1.2 THESIS OUTLINE

In Chapter 2 background information is given of the physiology and complementary mechanics of the cardiac tissue. The passive HO and active TVE constitutive models are described in Chapter 3. The implementation of these constitutive models in the user subroutine UMAT is described in Chapter 4. The methods of the verification and reality-check test-cases are described in Chapter 5. The corresponding results are described and discussed in 6. Finally, the general discussion and conclusions are presented in Chapter 7.

2 | ANATOMY, PHYSIOLOGY AND MECHANICS OF THE HEART

In the first part of this chapter the anatomy and physiology of the heart are briefly touched upon on macro- and microscale. In the second part, the coupling between the anatomical, physiological and mechanical characteristics of the cardiac tissue are discussed. Knowledge of these characteristics is important for the development and verification processes of the material model.

2.1 CARDIAC CYCLE

The cardiac cycle consists of a single heartbeat and can be divided in the relaxation phase (**diastole**) and the contracting phase (**systole**). Both phases have two stages, each stage ends with the opening or closing of either the atrioventricular valves (AV), located between the atria and ventricles, or the semilunar valves (SL), located downstream of the ventricles (Fig. 2.1).
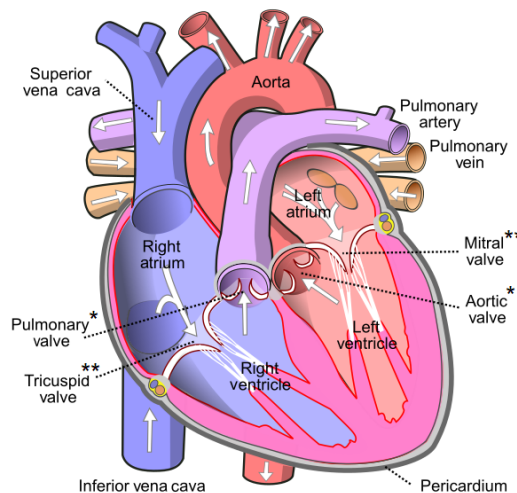

Figure 2.1: Schematic picture of the heart showing the location of the SL* valves (pulmonary and aortic valve) and the AV** valves (mitral and tricuspid valve). (Adapted from website [10])

The diastole begins with the **isovolumetric relaxation**. During this stage all valves are closed while the ventricles relax. This causes the ventricular volume to remain constant while the ventricular pressure declines. Subsequently, as a result of the atrial pressure exceeding the ventricular pressure the AV valves open, after which the **ventricular filling** stage begins. The venal blood pressure and atrial contraction causes blood from the venous system to stream into the ventricles, while the ventricles remain in a relaxed state. This ensures an increase in volume while the ventricular pressures remain the same. At the next stage, the **isovolumetric contraction**, the ventricles contract, causing the intraventricular pressure to rise and the AV valves to close. Because both the AV and SL valves are closed while the contraction takes place, the intraventricular pressure rises further, until the SL valves open. This marks the ending of the isovolumetric contraction and the beginning of the **ventric-**

ular ejection. Due to the pressure build-up from the isovolumetric ejection stage, and the ongoing contraction, the blood flows into the pulmonary artery and aorta causing the ventricular volumes to decrease. An overview of the four stages with their corresponding pressure-volume relation are visualised in the left ventricular pressure-volume (PV) loop in Fig. 2.2.
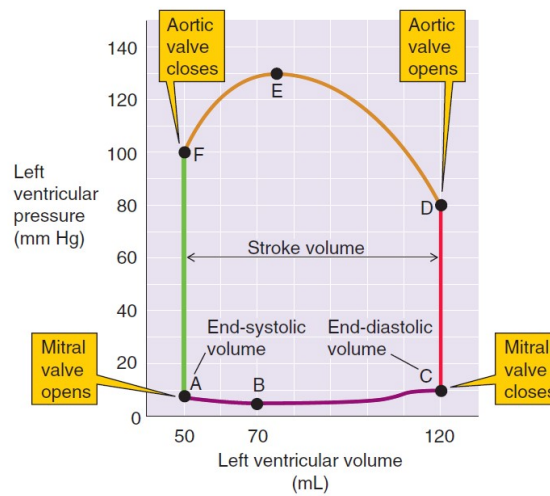

Figure 2.2: Physiological PV loop of the left ventricle (LV). The two stages of the diastole are depicted, i.e. (F-A) isovolumetric relaxation and (A-C) ventricular filling. Also, the two stages of systole are depicted i.e., (C-D) isovolumetric contraction and (D-F) ventricular ejection. B depicts the point with the lowest pressure, E depicts systolic peak pressure. Obtained from [11].

Frank–Starling Relation

The stroke volume (SV) is dependent on multiple parameters, i.e. venous return (preload), vascular resistance (afterload) and contractility (inotropy). The Frank-Starling (FS)-mechanism is the ability of the heart to adjust its contractility as response of changes in venous return in a beat-to-beat manner [12]. This can be visualised by the FS-curve (Fig. 2.3). This shows that the preload influences the force of the stroke volume. However, there is no single FS-curve, but a family of FS-curves. The FS-curves can be seen as a measure of the contractile cardiac state. For example, one has a 'higher' FS-curve when one is sporting, or a 'lower' FS-curve if one has heart failure. Additionally, the effect of an increase of the afterload will on short term result in less stroke-volume. However, after a short while (1-2 min), the contractility of the heart will increase, causing the SV to return to its initial value [12].

The mechanism behind the FS-relation can be explained as follows. Due to increased venous return, the ventricular volume increases as well, resulting in an increased initial length of the cardiac muscle fibre (especially the sarcomeres) before the contraction. With increasing sarcomere lenght, the sarcomeres become more sensitive to $[Ca^{2+}]$, as a result they can contract with more force [12]. The increased force generation enables the heart to eject the additional venous return, consequently increasing the stroke volume.
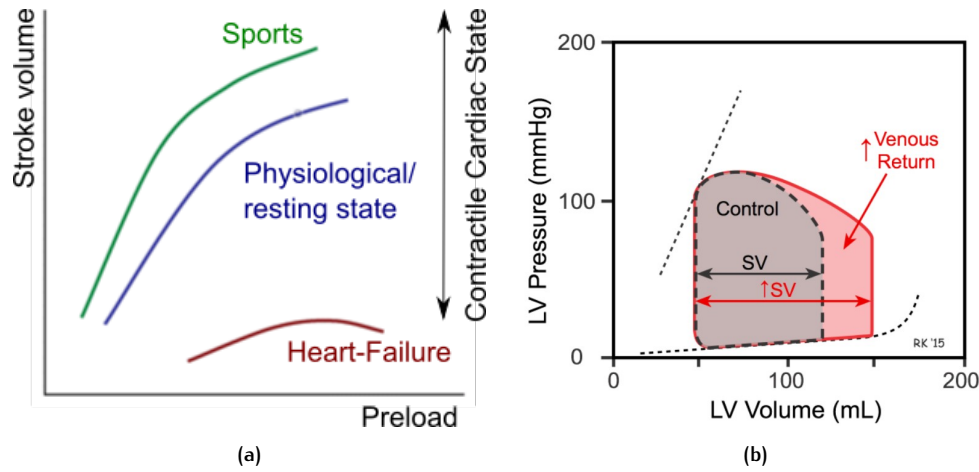
Figure 2.3: (a) A family of FS-curves, describing the contractile cardiac function. The blue line, depicting a physiological, resting state contractile cardiac state, describes the influence of the pre-load on the contractility of the heart in a beat-to-beat manner (the latter measured by the stroke volume). Under higher demand, e.g. sporting, the FS-curve moves up and left on the graph. With certain diseases, e.g. heart-failure, the FS-curve moves down and right. (Adjusted from [13]). (b) Direct influence of the venous return on the PV loop, assuming there is no inotropic or afterload reaction on the increase in venous return. SV = stroke volume. (Obtained from website [14]).

2.2 CARDIAC TISSUE BIOMECHANICS

In a material model the behaviour of the material is defined by a constitutive law. This law describes the relation between stress and strain within the model, usually as a response on an applied load or displacement. In-vivo this response is defined by the micro-architecture of the cardiac tissue. In this thesis, the cardiac tissue is assumed to have nonlinear, hyperelastic, orthotropic, incompressible behaviour. This section gives a brief overview of the current knowledge of the in-vivo working mechanisms behind these material characteristics.

2.2.1 Passive Component: The Tissue Micro–Architecture

The mechanics of the cardiac tissue are mainly dependent on its micro-structure. The heart wall consists of three distinct tissue layers. The external layer called the epicardium, and the internal layer called the endocardium, consist of mainly epimysial collagen and elastin. Additionally, the inside of the endocarium is covered with endothelial cells to form a barrier between the cardiac tissue and the blood within the heart. The middle layer, called the myocardium, is the muscle layer and consists volumetricly of 70% of cardiac muscle cells (cardiomyocytes), forming an important structural component of the cardiac tissue. The other 30% consists of multiple extracellular components, of which 2-5% is composed of collagen [8]. Cardiomyocytes are attached to each other in series via intercalated disks, forming muscle fibres. Multiple muscle fibres in parallel form layers (or sheets) of 4 cells thick, with extensive cleavage planes in between sheets. Due to the branching nature of the cardiomyocytes the cardiac tissue has a local preferred fibre direction, rather than a strict single fibre direction. The cardiomyocytes are kept together by means of collagen, which despite its small volume has an important structural function in the extracellular matrix. It has been classified into three components [15]. The epimysial collagen (or epimysium) surrounds the entire muscle, as it forms the biggest part of the epi- and endocardium. Secondly, the perimysial collagen (or perimysium) enables a loose connection between adjacent muscle sheets and span-

ning cleavage planes. The loose form of connection enables a substantial amount of sliding between adjacent muscle sheets [16]. Lastly, the endomysial collagen (or endomysium) surrounds and connects individual cardiomyocytes. A schematic overview of the muscle and collagen fibres is shown in Fig. 2.4. Other components of the cardiac tissue are the capillary network, fibroblasts and polyglycosaminoglycans [17].
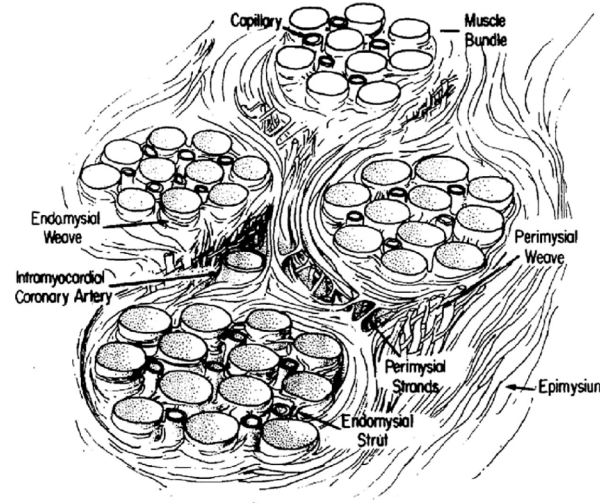

Figure 2.4: Schematic drawing of the collagen network of the cardiac tissue. The epimysial collagen surrounds the entire muscle, the perimysial collagen enables loose connection in between cleavage planes and between adjacent muscle sheets (in the figure depicted as the 'muscle bundle') and cleavage planes and the endomysium surrounds individual cardiomyocytes. Also arteries are shown. (Obtained from [18]).

Hyperelastic and Orthotropic Behaviour

The cardiac tissue has shown hyperelastic and orthotropic behaviour [8]. The mechanism behind the hyperelastic behaviour can be explained looking at the schematic figure of muscle and collagen fibres (Fig. 2.5), where the depicted collagen fibres represent endo- and perimysial collagen. In the case of tension, both muscle and collagen fibres are under tension. As the cardiac tissue is more under tension, the collagen fibres undergo stress stiffening, causing nonlinear behaviour. Myocardial fibres cannot withhold compression and consequently show buckling behaviour. This causes lateral stretching of the collagen fibres. It is suggested that this mechanism justifies the relatively high compression stiffness which is observed in cardiac tissue [8].

The mechanism of the orthotropic behaviour of the cardiac tissue is visible in Fig. 2.5, where three main directions can be distinguished. Definition of the three orthotropic directions is done in Fig. 2.6 (d) and (e). The first axis coincides with the main muscle fibre direction (f_0). The second axis (s_0) is orthogonal to f_0 within the muscle sheet plane, taking into account the mechanical properties of the peri- and endomysial collagen. The last axis is taken normal to the $f_0 - s_0$ plane (n_0).
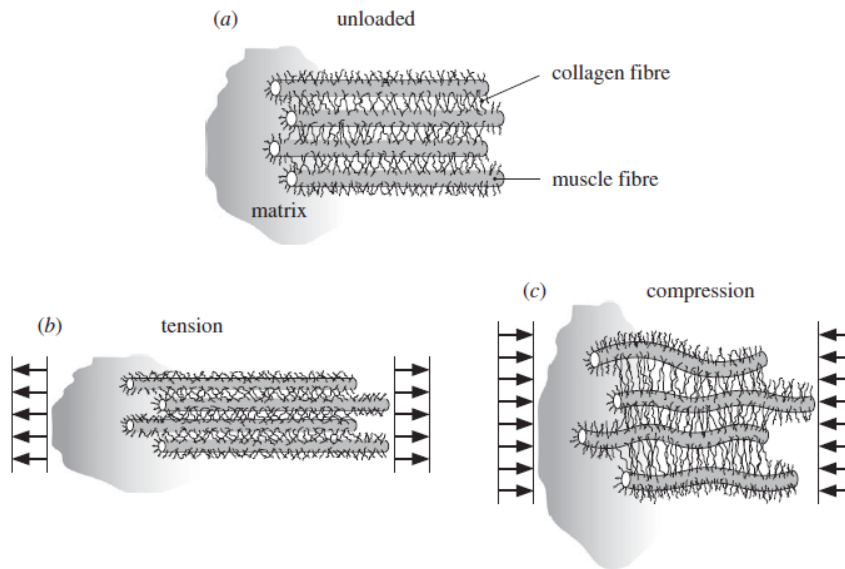
Figure 2.5: Schematic description of the muscle fibres, collagen fibres and extracellular matrix. The collagen fibres in this figure represent endo- and perimysial collagen. (a) Unloaded cardiac tissue. (b) During stretch of the cardiac tissue, muscle fibres give resistance as well as the collagen fibres. The stress-stiffening is caused by the recruitment of the collagen fibres, causing the nonlinear behaviour of the cardiac tissue. (c) Muscle fibres cannot resist compression loading (buckling occurs), while the collagen fibres are visibly stretched. (Obtained from [8]).

Local Fibre Orientation

The muscle fibres are not in a parallel position relative to the heart wall. Rather, the orientation of the muscle fibres varies transmurally between +50 and +70 degrees in the epicardium region, 0 degrees in the mid-wall region and -50 to -70 degrees in the endocardium region [8] (Fig. 2.6 (b)). This results in varying mechanical properties in different depths of the cardiac tissue. Thus, the orthogonal material behaviour applies to the myocardium when used with a local coordinate system.

Compressibility

The first cardiac tissue models assumed incompressibility of the cardiac tissue. This assumption was made because the components of the cardiac tissue (e.g. collagen fibre, muscle fibre, ground substance) were mainly consisting of water. Although the water could move in and out of the tissue, this movement was assumed to be so slow that its volumetric effects were assumed negligible [19]. In the 1990's, experiments on perfused passive myocardium of rats showed that passive cardiac tissue is compressible [19]. In 2002, in-vivo experiments on ovine hearts showed that the cardiac tissue shows incompressibility during the diastole and compressibility during the systole [20]. Additionally, a recent study with similar methods of the 2002 study showed that the volume change varied in different regions of the heart, as well as the volume-change was transient throughout the cardiac cycle [21] (Fig. 2.7). Additionally, [22] presented that a model with a compressibility-condition during systole accounted for a reduction in peak-stresses of 50% as compared to a model with a incompressible-condition. However, because of simplicity reasons, incompressibility is still assumed in the current model.
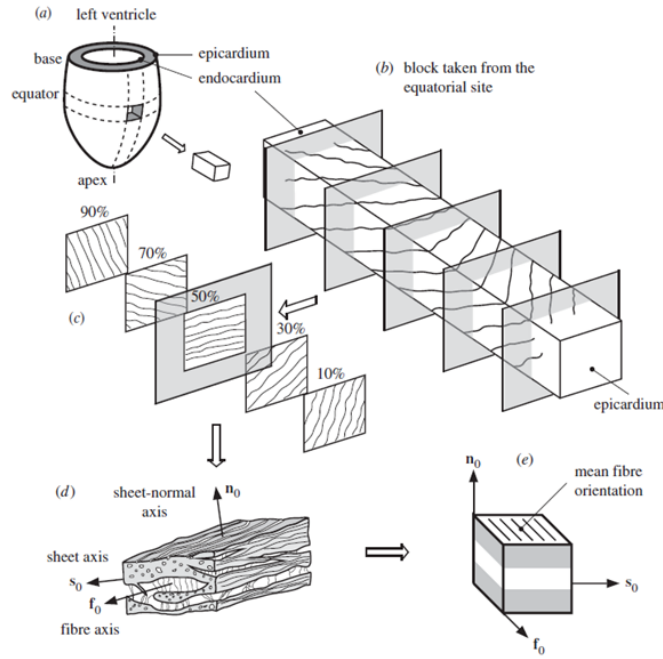
Figure 2.6: (a) Simplified left ventricle. (b) Muscle fibre structure, which varies in different layers of the heart ventricle. (c) Muscle fibre direction in circumferential-longitudinal planes of 5 different depths of the wall thickness. (d) The local coordinate system is coupled to the cardiac tissue structure, with the muscle fibre axis ($\mathbf{f}_0$), the collagen fibre axis ($\mathbf{s}_0$) and the normal axis ($\mathbf{n}_0$) to these two fibres. (e) single element model (SEM) of cardiac tissue with local coordinate system. (Obtained from [8]).
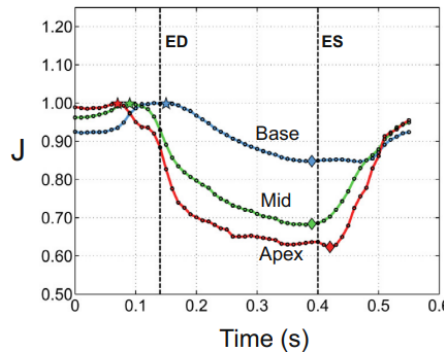
Figure 2.7: In vivo measured volume change of cardiac tissue (J) during the whole heart cycle in a healthy ovine heart. (Obtained from [21]).

Viscosity

During mechanical experimental tests the cardiac tissue show hysteresis (e.g. [23], [24]), and therefore the tissue can be described as viscoelastic. The exact mechanism of viscoelasticity is still under discussion, but it is believed that the viscoelastic behaviour can be attributed to a combination of proteins occurring in the cardiac cells and extracellular matrix [25], [26]. Generally in the cardiac FE modelling community the viscosity in cardiac tissue is assumed negligible. However, there exist computational cardiac applications that include viscosity. The most recent viscoelastic orthotropic model is developed by [27] and repeated by [28]. However, there was not yet found a good material parameter fit. As it is not considered within the scope of this master thesis to improve on this model, the viscosity is not included in the material model discussed in this thesis.

2.2.2 Active Component: The Cross-Bridge Cycle

Cardiac tissue is part of a living being, meaning that next to the passive behaviour the tissue can change over time. These active changes can be divided into two mechanism types. On the one hand, the reference configuration can change for a short period of time (few seconds to minutes), e.g. the contraction of a muscle fibre. On the other hand, the reference configuration can change permanently over a longer period of time, e.g. regrowth and remodelling of the tissue. In this thesis the active component is defined as the reversible type of active change over a short period of time, specifically the contraction of the cardiac tissue.

In section 2.2.1 the microstructure of the cardiac tissue is mentioned to consist of muscle fibres and collagen fibres, forming sheets of which the cardiac muscle is composed. The mentioned muscle fibre is contractile, and consists of multiple cardiac muscle cells connected via intercalated discs. The cardiac muscle cells are striated, branching, and generally have just one nucleus (Fig. 2.8). Striation in a muscle cell is the outing of the highly structured thick and thin filaments, which are the driving force behind the muscle contraction. A sarcomere is the smallest functional entity of the cardiomyocyte, consisting of a thick and a thin filament. During a contraction, the thin filaments are forced to slide over the thick filaments causing a shortening. Because the neurons coordinate the contraction of all the sarcomeres, they shorten roughly at the same time, causing the contraction of the whole muscle [11]. A single shortening of the sarcomere is called a cross-bridge cycle, and is explained in more detail below.
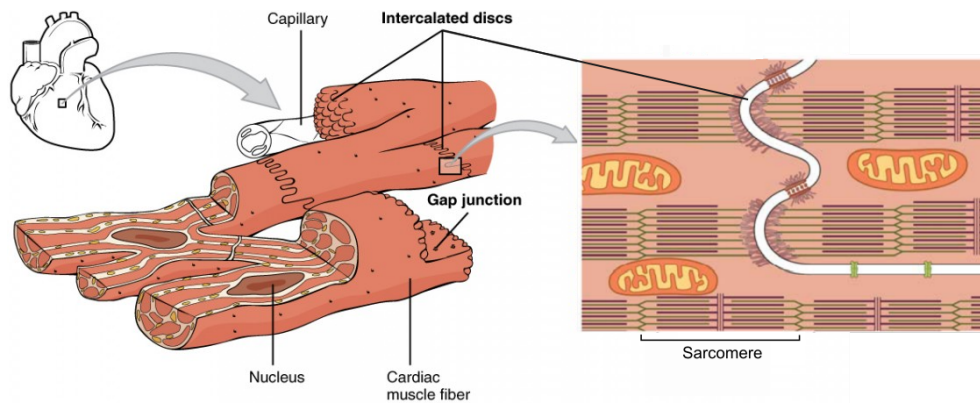
Figure 2.8: Microstructure of the cardiomyocyte, showing the branching nature of the cardiomyocytes. It also shows the strands of sarcomeres, which arranged in parallel form the structural basis of the cardiomyocytes. (Adapted from [29]).

The thick and thin filaments of the sarcomere consist of myosin and actin proteins, respectively. During a cross-bridge cycle (Fig. 2.9) the myosin head binds to the actin filament forming a cross-bridge. Hydrolysis of ATP causes the myosin head to contract, causing the thin filament to slide past the thick filament. This is called the power-stroke. Finally, the myosin head detaches from the actin filament. The whole cross-bridge process is initiated and maintained by the transient increase of the intracellular $[Ca^{2+}]$ caused by an action potential delivered by the neural network. A decrease in the intracellular $[Ca^{2+}]$ causes relaxation of the sarcomere [11].
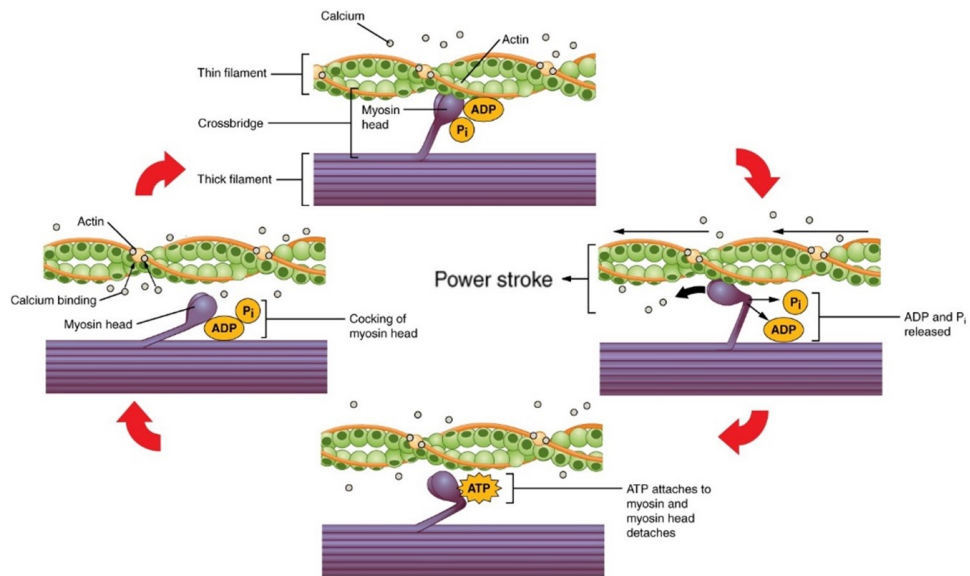
Figure 2.9: Schematic of the sarcomere cross-bridge cycle. Left: marks the relaxed myosin head. Above: marks the attachment of the myosin to the actin filament. Right: the ATP that is attached to the myosin head undergoes a hydrolysis reaction, causing the power stroke of the sarcomere. Below: a new ATP molecule attaches to the myosin head causing the myosin head to detach of the actin filament. (Adapted from website [30]).

Opposing actin filaments can have overlap. At the locations of overlap, there is no place for the myosin heads to bind to the actin filaments. On the other hand, if the sarcomere is stretched very much, the myosin heads will also have less attachment points of the actin filament available. Consequently, the optimal sarcomere length working range at which the sarcomere performs optimally is between 1.8 and 2.3 μm (Fig. 2.10) [31].
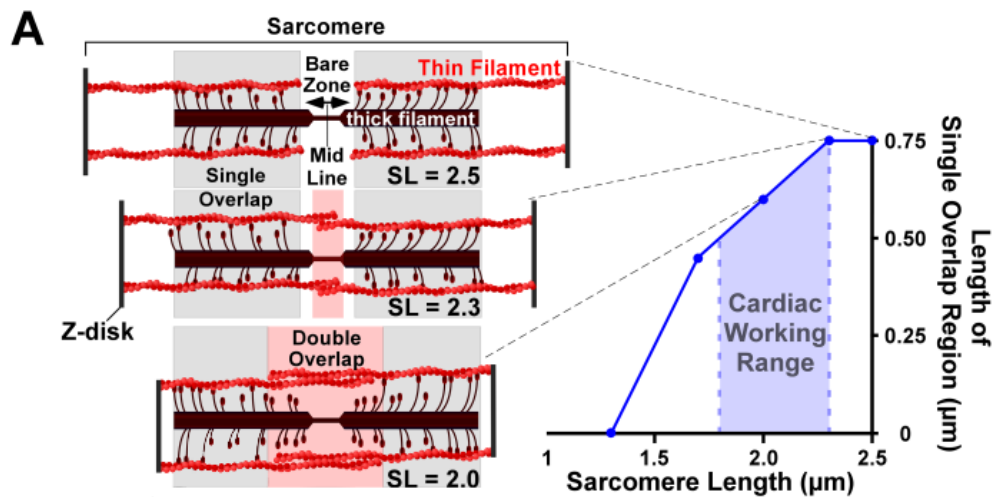
Figure 2.10: The optimal sarcomere length working range is between 1.8 and 2.3 μm. The borders of this optimal working range are located at the points that the amount of bare zone, or the amount of double overlap cause the myosin heads to have less area to attach themselves to the actin filaments. (Adapted from [31]).

3 | CONSTITUTIVE MODELLING

The hyperelastic, orthotropic, incompressible behaviour of the myocardium as described in Chapter 2, is represented by a constitutive law. Mechanically, the material properties of the myocardium can be decomposed in a passive component corresponding to the mechanical properties of the myocardium in relaxation, and an active component corresponding to the contractile properties of the myocardium. Following an active stress approach [17], the active stress component is added to the passive stress component resulting in

$$\boldsymbol{\sigma} = \boldsymbol{\sigma}_{pas} + \boldsymbol{\sigma}_{act}. \tag{3.1}$$

In this thesis the passive constitutive law was defined by the HO model [8]. Furthermore, the active constitutive law was defined by the TVE model [9], [32]. Both are discussed in more detail in sections 3.1 and 3.2, respectively.

3.1 PASSIVE COMPONENT: HOLZAPFEL AND OGDEN MODEL

In the past decades, multiple material models are developed to approximate the passive mechanical behaviour of cardiac tissue. This paragraph provides a brief overview of the development of passive cardiac material models. Initially, passive cardiac material behaviour was modelled in an isotropic manner, e.g. [33]. Subsequently, to account for anisotropy of the myocardium, transverse isotropic material models have been developed e.g. [34], [35], [36], [37]. At a certain point in time, cardiac tissue was found to have orthotropic properties, mainly due to the work of [38]. Consequently, orthotropic models have been developed. Initially, this was done in the 'pole-zero' model by [39]. Following, orthotropic models based on Fung-type constitutive equations were developed by [40] and [41]. A currently much-used material model for passive cardiac tissue is the invariant-based HO model. This model considers orthotropic, hyperelastic, incompressible behaviour and includes eight parameters correlating to the structure of the cardiac tissue. However, viscoelasticity is not taken into account. For a more detailed review of existing passive cardiac material models, the interested reader is referred to [8] and [17].

In this thesis the HO model was used as passive material model because of the following reasons. First, the HO model is a phenomenologically informed model (based on experimental data). Additionally, it includes information of the macroscopic morphological structure of the cardiac tissue, e.g. the invariants representing the extracellular matrix ($\bar{I}_1$) and the fibre- and collagen-mechanics ($\bar{I}_{4f}, \bar{I}_{4s}, \bar{I}_{8fs}$) [8]. As it does not include microscopic morphological information, it cannot be defined as a structurally informed model (as defined by [17]). However, it may be considered being in between a phenomenological and a structural model, as it forms a balance between the micro-structurally informative but complicated and hard to work with structural models, and the less micro-structurally informative but easier to work with phenomenological models. Second, Holzapfel et al. [8] show that when material parameters are positive, the strain energy function (SEF) is convex. Also, the model is consistent with inequalities required for strong ellipticity. Convexity and ellipticity are important factors for material model stability. Lastly, the HO model is orthotropic, as it is introduced on the basis of fibre-directions $\mathbf{f}_0, \mathbf{s}_0, \mathbf{n}_0,$

which is important to represent the in-plane nonisotropic behaviour perpendicular to the fibre-direction and the possible mechanical interaction between fibre- and sheet-direction.

3.1.1 HO Constitutive Law

The constitutive law of HO is defined by the hyperelastic strain energy function (SEF) Ψ in the paper, of which the first component embodies the volumetric behaviour and the last three components the isovolumetric behaviour. It is defined by [8] as follows

$$\Psi(\mathbf{C}) = \underbrace{\frac{\kappa}{2}(J-1)^2}_{\Psi_{vol}} +$$

$$\underbrace{\frac{a}{2b}exp[b(\bar{I}_1 - 3)] + \sum_{i=f,s}\frac{a_i}{2b_i}(exp[b_i(\bar{I}_{4i} - 1)^2] - 1) + \frac{a_{fs}}{2b_{fs}}(exp[b_{fs}(\bar{I}_{8fs})^2] - 1)}_{\Psi_{isovol}},$$

$$(3.2)$$

where a, a_f, a_s and a_{fs} are stress-like material parameters, b, b_f, b_s and b_{fs} are dimensionless material parameters, κ represents the bulk modulus and J the determinant of the deformation gradient ($det(\mathbf{C})$). The invariants are defined as

$$\bar{I}_1 = tr(\overline{\mathbf{C}}), \qquad \bar{I}_{4f} = \mathbf{f_0}\overline{\mathbf{C}}\mathbf{f_0}, \qquad \bar{I}_{4s} = \mathbf{s_0}\overline{\mathbf{C}}\mathbf{s_0}, \qquad \bar{I}_{8fs} = \mathbf{f_0}\overline{\mathbf{C}}\mathbf{s_0}, \qquad (3.3)$$

where $\mathbf{f_0}$ and $\mathbf{s_0}$ are the fibres in fibre- and sheet-direction, denoted as

$$\mathbf{f_0} = \begin{bmatrix} 1 & 0 & 0 \end{bmatrix}^T \qquad = \text{ fibre direction in reference configuration,} \qquad (3.4)$$

$$\mathbf{s_0} = \begin{bmatrix} 0 & 1 & 0 \end{bmatrix}^T \qquad = \text{ sheet direction in reference configuration.} \qquad (3.5)$$

In the SEF of HO the isotropic invariant $\bar{I}_1$ is related to the mechanical behaviour of the non-collagenous and non-muscular interstitial matrix of the cardiac tissue, including the fluids. The muscular and collagen mechanical behaviours in fibre- and sheet-directions are represented by invariants $\bar{I}_{4f}$ and $\bar{I}_{4s}$, respectively. Lastly, $\bar{I}_{8fs}$ represents the interaction between the mechanics in fibre- and sheet-directions [8]. Similarly, the local orientation used in this thesis was based on the tissue architecture of the myocardium (Figure 2.6). The first axis coincided with the myofibres ($\mathbf{f_0}$). The second axis ($\mathbf{s_0}$) was taken orthogonal to $\mathbf{f_0}$ in the direction of the plane layer, also called sheet, which took into account the mechanical properties of the endo- and perimysium. The last axis was taken normal to the $\mathbf{f_0} - \mathbf{s_0}$ plane ($\mathbf{n_0}$).

3.1.2 HO Material Parameters

Material parameters used in Holzapfel et al. [8] are based on porcine experimental triaxial shear data (n = 6) by Dokos et al. [23]. A more recent publication of Sommer et al. [24] presents data of biaxial tensile and triaxial shear tests on human cardiac tissue (n = 18). Material parameters based on the latter shear data are determined by Sack et al. [42]. When comparing behaviour of the two sets of material parameters, Sack et al. [42] found that the material parameters based on the porcine data results in much stiffer material behaviour, particularly in the fibre direction. Sack et al. [42] consider the data of human specimens more reliable, because in Sommer et al. [24] more advanced methods are used to prevent muscle contraction. The material parameters of Sack et al. [42] based on cardiac experimental data of human specimens were used in this thesis.

Table 3.1: Material parameters derived from human experimental data (n=18) [24] by [42] and porcine (n=6) experimental data [23].

tissue	a (MPa)	b (-)	a_f (MPa)	b_f (-)	a_s (MPa)	b_s (-)	a_{fs} (MPa)	b_{fs} (-)
Porcine	0.000261	10.767	0.019539	13.615	0.003406	5.6523	0.000313	14.068
Human	0.001051	7.542	0.003465	14.472	0.000481	12.548	0.000283	3.088

3.1.3 HO Stress Tensor

The Cauchy stress tensor of the HO model is defined explicitly by [8]. In this article the Cauchy stress tensor of the HO model, which can be decomposed in a volumetric σ_{vol} and isovolumetric σ_{isovol} part, is defined explicitly as

$$\sigma = \underbrace{-p\mathbf{I}}_{\sigma_{vol}} + \underbrace{2\psi_1\mathbf{B} + 2\psi_{4f}(\bar{\mathbf{f}} \otimes \bar{\mathbf{f}}) + 2\psi_{4s}(\bar{\mathbf{s}} \otimes \bar{\mathbf{s}}) + \psi_{8fs}(\bar{\mathbf{f}} \otimes \bar{\mathbf{s}} + \bar{\mathbf{s}} \otimes \bar{\mathbf{f}})}_{\sigma_{isovol}}. \tag{3.6}$$

The definition of the HO Cauchy stress tensor includes $\psi_1, \psi_{4f}, \psi_{4s}$ and ψ_8, which are the first derivatives of the SEF Ψ with relation to the isochoric invariants (explicitly written out in Appendix A). The Cauchy stress tensor also includes the penalty parameter, defined as [43]

$$p = \frac{\partial \Psi_{vol}}{\partial J} = \kappa(J - 1), \tag{3.7}$$

where κ denotes the bulk modulus. Additionally, the isovolumetric deformation gradients in fibre and sheet directions in current configuration are defined as

$$\bar{\mathbf{f}} = \bar{\mathbf{F}}\mathbf{f}_0 \qquad\qquad = \text{ fibre direction in current configuration,} \tag{3.8}$$

$$\bar{\mathbf{s}} = \bar{\mathbf{F}}\mathbf{s}_0 \qquad\qquad = \text{ sheet direction in current configuration.} \tag{3.9}$$

3.2 ACTIVE COMPONENT: TIME–VARYING ELASTANCE MODEL

The active part of the cardiac tissue behaviour in this thesis was defined by the TVE model of [9]. This choice was made based on the following considerations. The TVE model includes the FS-effect, describing the increase of contraction force as a result of increased blood inflow. Similarly, it takes into account biophysical events within the cell membrane, i.e. free calcium transient, Ca^{+2}-troponin interaction and cross-bridge cycling. Also, cell-deactivation is included, of which the importance for modelling was emphasised by [44]. Additionally, experiments of [9] showed that the model can accurately predict tension development of isometric and isotonic experiments. Lastly, by optimising the maximal contraction stress and the active fibre-sheet interaction, patient-specific modelling is possible [32]. Limitations of the model need to be discussed as well. The force-velocity relationship of the cardiac cell contraction [9] is absent. Despite the absence of the force-velocity relationship, [9] stated that the TVE model could accurately model the mechanisms of the ventricular contraction at end-systole. Also, the model parameters are mainly based on experiments done on rat cardiac tissue, as no human based experimental data of active cardiac tissue behaviour is available [9].

3.2.1 TVE Stress Tensor

Following Guccione et al. [9] and Sack et al. [32], the active stress of the material law is defined by the TVE model. In this model the stress production of an action potential is dependent on the time, t initial sarcomere length $l(E_{ff}^G)$ and the peak intracellular calcium concentration $Ca_{0_{max}}$ (the latter is taken as a constant), resulting in the following equation of the active Cauchy stress tensor

$$\sigma_{af}(t, E_{ff}^G) = \frac{T_{max}}{2} \frac{Ca_0^2}{Ca_0^2 + ECa_{50}^2(E_{ff}^G)} (1 - cos(\omega(t, E_{ff}^G))). \tag{3.10}$$

The active Cauchy stress tensor includes the length-dependent calcium sensitivity (ECa_{50}) and step-function ω, which are defined by

$$ECa_{50} = \frac{Ca_{0_{max}}}{\sqrt{exp[B(l(E_{ff}^G) - l_0) - 1]}}, \tag{3.11}$$

and

$$\omega(t, E_{ff}^G) = \begin{cases} \pi \frac{t}{t_0} & \text{when } 0 \leq t \leq t_0, \\ \pi \frac{t - t_0 + t_r(l(E_{ff}^G))}{t_r} & \text{when } t_0 \leq t \leq t_0 + t_r(l(E_{ff}^G)), \\ 0 & \text{when } t \geq t_0 + t_r(l(E_{ff}^G)), \end{cases} \tag{3.12}$$

where t_0 is the time-to-peak tension and t_r is a function dependent on the sarcomere length (l) defined as follows

$$t_r(l(E_{ff}^G)) = ml(E_{ff}^G) + b, \tag{3.13}$$

of which m and b are constants. The sarcomere length (l) is defined as a function dependent on the initial sarcomere length (l_r), given by the Green-Lagrangian strain tensor in fibre direction E_{ff}^G.

$$l(E_{ff}^G) = l_r \sqrt{2E_{ff}^G + 1}. \tag{3.14}$$

The active tension in sheet-direction (σ_{as}) is related to the active tension in fibre-direction (σ_{af}) by a scaling value n_s, as shown in the following equation

$$\sigma_{as} = n_s \sigma_{af}. \tag{3.15}$$

The n_s parameter has a value between 0.0 and 1.0 and represents the interaction with the neighbouring muscle fibres. When implemented in a whole heart model, this value will affect both the contractility and the degree of twist developed in the chamber during the contraction of the heart.

3.2.2 TVE Material Parameters

The TVE model describes a quick increase of active tension until peak tension is reached at time-point t_0. After this point a slower decrease back to zero active tension is defined, representing the relaxation time of the action potential. The used parameters for the active tension in fibre direction, given by Eq. 3.10 - 3.14 are shown in Table 3.2. The parameters were obtained by [9] by optimising the TVE model to agree as closely as possible to active tension development observed in right ventricular rat trabeculae of which most data were obtained from the group of Ter Keurs: [45], [46], [47], [48] and [49]. Parameters regarding the isotonic tension-sarcomere shortening velocity relation were derived from an article of [50], which showed the results of experiments done on right ventricle trabeculae from rat hearts. Note that the T_{max} value denotes the maximal contractility. This value can be optimised to achieve realistic contractility, as was done in [32]. However, this was not yet done in this thesis, considering the stage of the development of the material model.

Table 3.2: Active material parameters as in Guccione et al. [9].

Parameter	Value	Unit	Description
T_{max}	0.1357	MPa	Isometric tension under max. activation
Ca_0	0.004350	mm	Peak intracellular calcium concentration
$Ca_{0,max}$	0.004350	mm	Maximum Ca_0
B	4750	mm^{-1}	Parameter governing shape of peak isometric tension-sarcomere length relation
l_0	0.00158	mm	Sarcomere length at which no active tension develops
lr	0.00191	mm	Stress-free sarcomere length
m	1048.9	s/mm	Slope of linear relaxation duration - sarcomere length relation
b	−1.429	s	Time-intercept of linear relaxation duration - sarcomere length relation
t_0	0.1	s	Time-to-peak tension
n_s	0.4	(-)	Scale, describing relation of stress in sheet direction relative to the fibre direction

4 | MODEL INTEGRATION IN ABAQUS

In the previous chapter, the HO and the TVE material models were outlined. These material models are not readily available in Abaqus. Therefore, the constitutive equations were incorporated through the user-defined material subroutine UMAT, which will be discussed further in this chapter.

A user subroutine allows the user to customise a wide variety of abaqus capabilities, e.g. the user can define a material's mechanical behaviour. Multiple user subroutines are available that can be used in combination with Abaqus. As the stress is the measure we want to compute, either UANISOHYPER_INV or UMAT would be a suitable choice. In this thesis the subroutine UMAT is chosen above the use of the simpler UANISOHYPER_INV because the UMAT provides more freedom to customise the material model, e.g. enabling the addition of the active properties (TVE model).

The compatibility of the UMAT within the computations of Abaqus is visualised in Fig. 4.1. Every iteration of the UMAT requires a deformation gradient from Abaqus, which returns the corresponding stress tensor and stiffness matrix (Fig. 4.2). However, when using a global or local coordinate system, a different deformation is given to the UMAT. Mitigation of this difference is discussed in section 4.1.1. Incorporation of the stress vector and elasticity tensor computation are subsequently discussed in section 4.1.2 and 4.1.3. Lastly, in section 4.2, a brief overview of the tips and tricks for working with UMAT acquired during this thesis will be given. This will hopefully be beneficial for future scientists as starting point to get more acquainted with the user subroutine UMAT defined in the computer language Fortran.
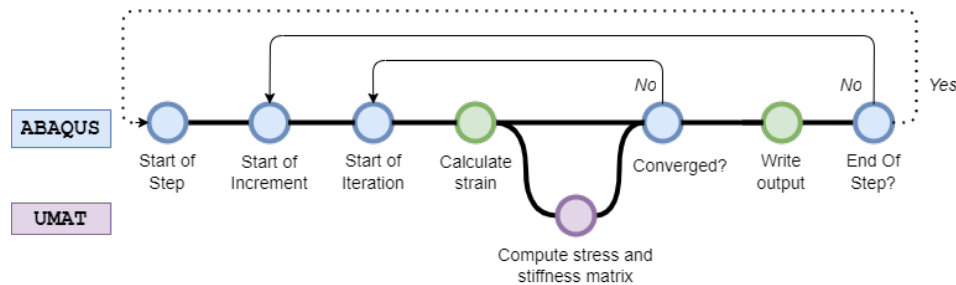

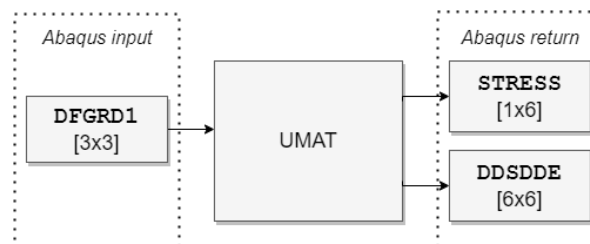**Figure 4.1:** Compatibility of UMAT in an Abaqus step.

Figure 4.2: Input and return tensors of UMAT.

4.1 UMAT REQUIREMENTS

4.1.1 Local Co–Rotational Coordinate System

As explained in section 2.2, the muscle fibre direction within the cardiac tissue varies transmurally. To incorporate such differences in muscle fibre direction in a whole heart model, a local coordinate system was used. Such a local coordinate system was defined by adding the `*Orientation` keyword to the Abaqus input file. The form of the deformation gradient passed to a user subroutine depends on the choice of coordinate system, i.e. local or global and the element type, e.g. shell or solid. When using a local coordinate system in combination with continuum elements in Abaqus/Standard the deformation gradient (`DFGRD1`) passed to the user subroutine has a 'Abaqus local deformation gradient' form, or $\mathbf{F}^{al}$ [51].

$$\mathbf{F}^{al} = \mathbf{R}^T \cdot \mathbf{F}^{EE} \cdot \mathbf{R} \qquad\qquad = \text{Abaqus local form} \qquad (4.1)$$

For a detailed step-by-step guide for the handling of this Abaqus local deformation gradient, the interested reader is referred to the paper of [52]. A short overview of this paper is given below.
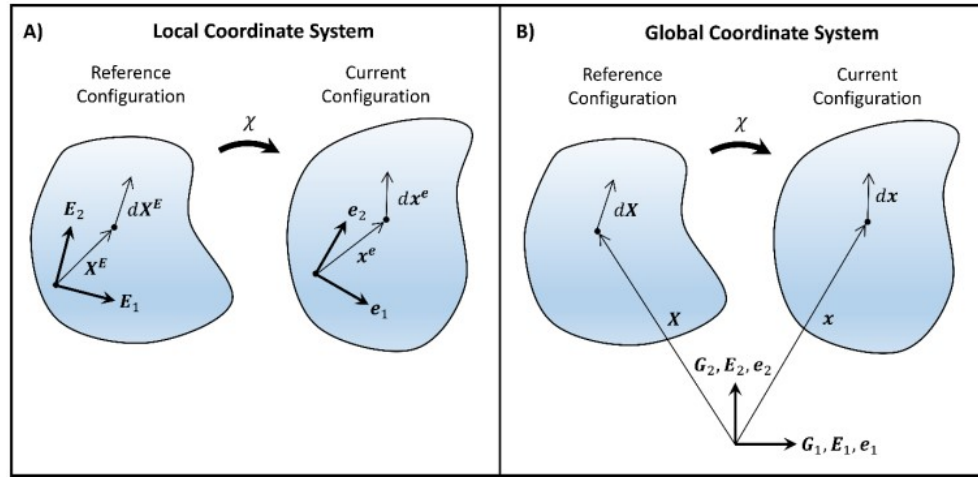

Figure 4.3: (a) The local coordinate system consists of a reference (E_i) and current (e_i) orthogonal coordinate system. These coordinate systems are dependent on the corresponding material orientation. (b) The global coordinate system is the same in all material points, as well as in reference and current configuration. (Obtained from [52]).

In continuum mechanics, one often refers to three orthogonal coordinate systems (Fig. 4.3): global (G_i), reference local (E_i) and current local (e_i). The global coordinate system has the same orientation in all material points, while the local coordinate system co-rotates with the material point to which it is assigned to, resulting in a reference and current configuration. Deformation gradients corresponding to these coordinate systems can be defined as below ([52]).

$$\mathbf{F}^{EE} = \mathbf{R} \cdot \mathbf{U} \qquad\qquad = \text{global form} \qquad (4.2)$$

$$\mathbf{F}^{eE} = \mathbf{U} \qquad\qquad = \text{co-rotational local form} \qquad (4.3)$$

These deformation gradients can be seen as the classical deformation gradients. However, when the keyword `*Orientation` is added to the Abaqus input file, the deformation gradient passed from Abaqus to the UMAT is in the $\mathbf{F}^{al}$ form (Eq. 4.1). The constitutive laws of HO and TVE are defined following the classical definition of the coordinate systems, and therefore the stresses should be derived using the co-rotational local deformation gradient Eq. 4.3. To do this with the given deformation gradient in $\mathbf{F}^{al}$ form, the steps below were followed.

1. Obtain rotation matrix ($\mathbf{R}$) via the polar decomposition of $\mathbf{F}^{al}$.

2. Compute the deformation gradient in local coordinate system: $\mathbf{F}^{eE} = \mathbf{F}^{al} \cdot \mathbf{R}^T$.

3. Compute $\sigma(\mathbf{F}^{eE})$.

4.1.2 Stress Tensor Computation

Section 3.1.1 describes the decomposition of the SEF in a volumetric and isovolumetric part (Eq. 3.2). The isovolumetric part must be incorporated analytically, as the SEF of HO is not readily available in Abaqus. Considering the (near) incompressibility assumption, the volumetric part can either be incorporated analytically or it can be computed by Abaqus. Incorporation of the volumetric and isovolumetric stress tensors in the user subroutine UMAT will be discussed in the paragraph below.

Analytical Incorporation of the (Iso)Volumetric Stress Tensor

The isovolumetric stress tensor was incorporated by including Eq. 3.6 and Eq. 3.10 in the Fortran script (provided in the supplementary material in Appendix A: *"CARD-MAT /_for /sigma..."*). The incompressibility assumption is embodied by the volumetric component of the stress tensor. Analytically (near) incompressibility can be enforced by assigning a value for the bulk modulus (κ in Eq. 3.2) with a value much higher than the shear modulus. In the Abaqus documentation the bulk modulus is advised to be taken 1E4 - 1E6 times as high as the shear modulus [53]. In the article of Prot et al. [54] a bulk modulus of κ = 1E5 MPa was suggested. However, a relative high bulk modulus is not beneficial for the numerical stability, often causing difficulties with the solution of the discretized equilibrium equations [55]. For this reason, in this thesis the isovolumetric part of the stress tensor and consequently the elasticity tensor were computed numerically by Abaqus.

Numerical Incorporation of the Volumetric Stress Tensor

For the incorporation of incompressible or nearly incompressible materials, Abaqus provides hybrid elements [53]. When a hybrid element is used in combination with user subroutine UMAT, Abaqus is programmed to compute the volumetric part of the stress tensor, and correspondingly adjust the elasticity tensor. There are three user material formulations defined that can be used in correspondance to hybrid elements. The default is the incremental formulation. This is suitable for material models that use an incremental Lagrange multiplier-based formulation of the SEF. In addition, the incompressible and total user subroutine formulations are available. The incompressible formulation is suitable for fully incompressible materials, and requires definition of only the isovolumetric component of the stress and elasticity tensor. The total formulation is suitable for nearly incompressible hyperelastic materials and for this the isovolumetric and volumetric response of the material needs to be defined separately and the volumetric response has to be derived from a SEF. Because the HO model is not a Lagrange multiplier-based formulation, and incompressibility was assumed (as specified in section 2.2), the incompressible user subroutine formulation was used.

To incorporate the incompressible user subroutine formulation, the Abaqus input file contained "`HYBRID FORMULATION=TOTAL`" behind the `*Material` keyword (.inp files are available in the supplementary material in Appendix A: *"CARD-MAT/_inp/..."*). Input files including this code were run directly by appointing the .inp file in the job, as the incompressible user subroutine formulation is not available in Abaqus/CAE.

4.1.3 Isovolumetric Elasticity Tensor

The elasticity tensor also needed to be defined in the user subroutine UMAT. It can be computed by either the analytical method, or numerically via the approximation method. Advantages of the approximation as compared to the analytical method, are the ease of incorporation and the lower risk of numerical instability. Theoretical advantages of the analytical method are the higher accuracy, and the lower computational cost. However, Liu et al. [56] found that computational cost of the approximation method can be higher or lower as compared to the analytical method, depending on the scale of the simulation and complexity of the SEF. Additionally, Liu et al. [56] found that the accuracy of both methods was comparable. In this thesis the elasticity tensor was computed by means of the approximation method. For completeness, both methods are described below.

Analytical Formulation

To implement the HO model analytically in the UMAT, the elasticity tensor was explicitly derived. The derivation of the elasticity tensor was mainly based on the work of [43]. The elasticity tensor is a fourth order tensor, which was defined by [43] as the second derivative of the SEF w.r.t. the right Cauchy-Green deformation tensor ($\mathbf{C}$), written as below

$$\mathbb{C} = 4\frac{\delta^2\psi(\mathbf{C})}{(\delta\mathbf{C})^2} = 2\frac{\delta\mathbf{S}(\mathbf{C})}{\delta\mathbf{C}}. \tag{4.4}$$

The first step of deriving the elasticity tensor analytically was the derivation of the second Piola-Kirchhoff stress tensor. This was defined by [43] as the first derivative of the SEF Ψ w.r.t. the right Cauchy-Green deformation tensor ($\mathbf{C}$), and could be written as follows

$$\mathbf{S} = 2\frac{\partial\Psi(\mathbf{C})}{\partial\mathbf{C}}. \tag{4.5}$$

Although with help of equations of [43] it is possible to derive this equation explicitly, there was found a more straight forward way. As the Cauchy stress derived from the HO SEF was known (Eq. 3.6), one could come by the second Piola-Kirchhoff stress by doing a pull-back operation ($\chi_*^{-1}[\bullet] = \mathbf{F}^{-1}[\bullet]\mathbf{F}^{-T}$) on the Cauchy stress and multiplying with the jacobian of the deformation gradient, which resulted in the following equation

$$\mathbf{S} = J\mathbf{F}^{-1}\sigma\mathbf{F}^{-T}, \tag{4.6}$$

which could be decomposed in a volumetric and isovolumetric part as follows

$$\begin{aligned}\mathbf{S} &= \mathbf{S}_{vol} + \mathbf{S}_{isovol} \\ &= J(\mathbf{F}^{-1}\sigma_{vol}\mathbf{F}^{-T} + \mathbf{F}^{-1}\sigma_{isovol}\mathbf{F}^{-T}).\end{aligned} \tag{4.7}$$

The elasticity tensor can be defined relating to the reference and current configuration. The reference configuration was obtained from Eq. 4.4, which was explicitly derived by [43] as

$$\mathbb{C} = \underbrace{J(\tilde{p}\mathbf{C}^{-1} \otimes \mathbf{C}^{-1} - 2p\mathbf{C}^{-1} \odot \mathbf{C}^{-1})}_{\mathbb{C}_{vol}} +$$

$$\underbrace{\mathbb{P} : \overline{\mathbb{C}} : \mathbb{P}^T + \frac{2}{3}J^{-2/3}(Tr(\overline{\mathbf{S}})\tilde{\mathbb{P}} - (\overline{\mathbf{C}}^{-1} \otimes \mathbf{S}_{isovol} + \mathbf{S}_{isovol} \otimes \overline{\mathbf{C}}^{-1}))}_{\mathbb{C}_{isovol}}. \tag{4.8}$$

In Eq. 4.8 the fictitious reference form of the elasticity tensor $\overline{\mathbb{C}}$ was defined by [43] as

$$\overline{\mathbb{C}} = 4\frac{\partial^2 \Psi_{iso}}{(\partial \overline{\mathbf{C}})^2},$$

(4.9)

the fictitious second Piola-Kirchhoff tensor was defined by [43] as

$$\overline{\mathbf{S}} = 2\frac{\partial \Psi_{isovol}(\overline{\mathbf{C}})}{\partial \overline{\mathbf{C}}},$$

(4.10)

and ψ_i'' are the second derivatives of the SEF w.r.t. invariants I_i (with $i = 1, 4f, 4s, 8$), which were explicitly written out in Appendix A. Also included in the elasticity tensor was scalar function $\tilde{p}$ [43], defined as

$$\tilde{p} = p + J\,dp/dJ = \kappa(2J - 1),$$

(4.11)

a modified projection tensor $\tilde{\mathbb{P}}$ of fourth-order defined by [43] as

$$\tilde{\mathbb{P}} = \mathbf{C}^{-1} \odot \mathbf{C}^{-1} - \frac{1}{3}\mathbf{C}^{-1} \otimes \mathbf{C}^{-1},$$

(4.12)

and a fourth order projection tensor w.r.t. reference configuration [43], defined as

$$\mathbb{P} = \mathbb{I} - \frac{1}{3}\overline{\mathbf{C}}^{-1} \otimes \overline{\mathbf{C}},$$

(4.13)

containing the fourth order unit tensor $\mathbb{I}$, which was written by [43] as

$$\mathbb{I} = \delta_{ik}\delta_{jl}\mathbf{e_i} \otimes \mathbf{e_j} \otimes \mathbf{e_k} \otimes \mathbf{e_l} = \mathbf{I}\overline{\otimes}\mathbf{I} = \mathbf{I} \odot \mathbf{I}.$$

(4.14)

Lastly, the tensor products $(:, \otimes, \underline{\otimes}, \overline{\otimes}$ and $\odot)$ were defined in Appendix A. Thereafter, the reference and current configurations of the elasticity tensor were related via multiplication with the inverse jacobian (J^{-1}) and a push-forward operation. Following [57], the current configuration of the elasticity tensor was found as follows

$$\mathfrak{c} = J^{-1}\chi_*(\mathbb{C}) = J^{-1}(\mathbf{F}\underline{\otimes}\mathbf{F}) : \mathbb{C} : (\mathbf{F}^T\underline{\otimes}\mathbf{F}^T).$$

(4.15)

To prevent the *Orientation command to affect the outcomes, the elasticity tensor needed to be defined via the Jaumann rate [58]. According to [54] and [59] the Jaumann rate was defined as follows

$$\tilde{\mathfrak{c}}^\tau = \mathfrak{c}^\tau + \check{\mathbb{C}}^\tau,$$

(4.16)

where $\tilde{\mathfrak{c}}^\tau$ was the spatial form of the elasticity tensor, dependent on the Kirchhoff stress τ, and $\check{\mathbb{C}}^\tau = \frac{1}{2}(\delta_{ik}\tau_{jl} + \delta_{jl}\tau_{ik} + \delta_{il}\tau_{jk} + \delta_{jk}\tau_{il})$. Note that the stress tensor of Abaqus was defined with the Cauchy stress. Consequently, by using the equation $\tau = J \cdot \sigma$, one could rewrite the Jaumann stress rate to be dependent on the Cauchy stress [54]

$$\tilde{\mathfrak{c}}^\sigma = J^{-1}\tilde{\mathfrak{c}}^\tau,$$
$$= \mathfrak{c} + \frac{1}{2}(\delta_{ik}\sigma_{jl} + \delta_{jl}\sigma_{ik} + \delta_{il}\sigma_{jk} + \delta_{jk}\sigma_{il}),$$

(4.17)

which could be used in the user subroutine. The elasticity tensor was defined as a fourth order tensor. Because the matrix contains major and minor symmetries, the fourth order tensor could be written in Voigt notation. The resulting 6x6 matrix below was returned as the DDSDDE [60].

$$\begin{bmatrix} \tilde{\mathbb{C}}^\sigma_{1111} & \tilde{\mathbb{C}}^\sigma_{1122} & \tilde{\mathbb{C}}^\sigma_{1133} & \tilde{\mathbb{C}}^\sigma_{1112} & \tilde{\mathbb{C}}^\sigma_{1113} & \tilde{\mathbb{C}}^\sigma_{1123} \\ \tilde{\mathbb{C}}^\sigma_{2211} & \tilde{\mathbb{C}}^\sigma_{2222} & \tilde{\mathbb{C}}^\sigma_{2233} & \tilde{\mathbb{C}}^\sigma_{2212} & \tilde{\mathbb{C}}^\sigma_{2213} & \tilde{\mathbb{C}}^\sigma_{2223} \\ \tilde{\mathbb{C}}^\sigma_{3311} & \tilde{\mathbb{C}}^\sigma_{3322} & \tilde{\mathbb{C}}^\sigma_{3333} & \tilde{\mathbb{C}}^\sigma_{3312} & \tilde{\mathbb{C}}^\sigma_{3313} & \tilde{\mathbb{C}}^\sigma_{3323} \\ \tilde{\mathbb{C}}^\sigma_{1211} & \tilde{\mathbb{C}}^\sigma_{1222} & \tilde{\mathbb{C}}^\sigma_{1233} & \tilde{\mathbb{C}}^\sigma_{1212} & \tilde{\mathbb{C}}^\sigma_{1213} & \tilde{\mathbb{C}}^\sigma_{1223} \\ \tilde{\mathbb{C}}^\sigma_{1311} & \tilde{\mathbb{C}}^\sigma_{1322} & \tilde{\mathbb{C}}^\sigma_{1333} & \tilde{\mathbb{C}}^\sigma_{1312} & \tilde{\mathbb{C}}^\sigma_{1313} & \tilde{\mathbb{C}}^\sigma_{1323} \\ \tilde{\mathbb{C}}^\sigma_{2311} & \tilde{\mathbb{C}}^\sigma_{2322} & \tilde{\mathbb{C}}^\sigma_{2333} & \tilde{\mathbb{C}}^\sigma_{2312} & \tilde{\mathbb{C}}^\sigma_{2313} & \tilde{\mathbb{C}}^\sigma_{2323} \end{bmatrix}$$

(4.18)

Note that because in this thesis hybrid elements were used in combination with the incompressible user subroutine formulation, only the anisotropic part of the stress and elasticity tensor needed to be computed for the implementation in the user subroutine UMAT.

Numerical Formulation

Another way of computing the elasticity tensor, as opposed to the analytical method explained above, is to approximate it numerically via the approximation method. This method is found to simplify the incorporation of complex constitutive models with comparable accuracy and computational efficiency, as compared to a closed form analytical solution [56]. The approximation method uses small perturbations in all directions of the deformation gradient, to compute the resulting change in stress with which the elasticity tensor can be approximated. For a more in detail explanation the reader is referred to the article of [7]. The approximation method was also used in [59], [61].

While obtaining the perturbed deformation gradient, perturbations in six independent directions were done. To this end, the (11), (22), (33), (12), (13) and (23) directions were used, which resulted in the following definition of the perturbed deformation gradient [61]

$$\hat{\mathbf{F}}^{(ij)} = \mathbf{F} + \Delta\mathbf{F}^{(ij)}, \tag{4.19}$$

where $\Delta\mathbf{F}^{(ij)} = \frac{\theta}{2}(\mathbf{e}_i \otimes \mathbf{e}_j\mathbf{F} + \mathbf{e}_j \otimes \mathbf{e}_i\mathbf{F})$. The numerically derived elasticity tensor was then defined by [61] as

$$\mathbb{C}_{ijkl} = \frac{I}{J\theta}[J_p^{(ij)}\sigma(\hat{\mathbf{F}}^{(ij)}) - J\sigma(\mathbf{F})]_{kl}, \tag{4.20}$$

where θ is the perturbation parameter, with a small value of $2 \cdot 10^{-8}$, $J = det(\mathbf{F})$, $J_p^{(ij)} = det(\hat{\mathbf{F}}^{(ij)})$ and σ is the full Cauchy stress.

The incorporation of the numerical calculation of the elasticity tensor by means of the approximation method in the user subroutine UMAT can be found in the supplementary material in Appendix A: *"CARD-MAT/_for/C_..."*.

4.2 DEBUGGING

UMAT is predominantly written with Fortran language. While working with the earliest fixed form of this language, minor mistakes (missing a space, having a 'tab' in stead of 6 spaces, etc.) can cause abortion of the job in Abaqus, while by modern standards it is not straightforward to debug. During this thesis three methods to debug the UMAT code were found to be useful. As a reference a short overview of these methods is given below. Another option is to use the free form of Fortran as opposed to the fixed form. The free form rules are less strict, making the process of coding less mistake-prone. However, it cannot be used in combination with the older fixed format of Fortran. To enable abaqus to read free source form Fortran, the code must start with the following text: `!dec$ freeform`. For additional tips and tricks for writing a user subroutine compatible with Abaqus, the interested reader is referred to [62].

State Variables, "STATEV"

UMAT has an array with solution-dependent state variables. These state variables are defined by the user by including the `statev(#)` command to the fortran script (where # can be any number). The state variables are computed every increment. When the number of solution-dependent state variables in the material definition matches the number of indices of the statev-array, all values of the state variables can be called by SDV (solution dependent state variables) in the field output of Abaqus.

".log" File

With certain mistakes in your UMAT, Abaqus will give an error. The location and nature of the error will appear in the ".log" file of your model. Additionally, with the `write(*,*)` command, UMAT returns the variable that is written behind this command to the .log file of your model at each iteration.

f2py

Lastly, the fortran file can be debugged via the 'Fortran to Python interface generator' abbreviated to f2py, which is a part of the Numpy package. With this utility, Fortran subroutines can be converted to python modules via e.g. the Anaconda prompt (command interface). These modules subsequently can be called in a python environment e.g. Spyder. Although the UMAT needs some small modifications to be used by f2py, the debugging with this utility is more sensitive then via the .log file provided by Abaqus, as it reacts to all the mistakes made in the Fortran file. Therefore, this was found to be the most effective way of debugging.

5 VERIFICATION METHODS

Verification of a material model assesses whether the theoretical constitutive law as discussed in Chapter 3 is accurately implemented. To verify the passive and active material model, the theory indicates to compare relevant outcomes computed by the model to either an analytical solution or a valid and verified benchmark solution. Accordingly, the verification of the passive material model consisted of comparing the stress and strain outcomes of defined test-cases to a benchmark solution comprising of the in-house developed UANISOHYPER_INV of the HO material model [63], as well as to the analytical solution. Stress results of the test-cases including both passive and active material properties were compared to an analytical solution.

To put the verification in practice, a verification single element model (SEM) (discussed in Section 5.1) underwent loads and boundary conditions of multiple test-cases (discussed in Section 5.2).

Additionally, during the development of a (FE) model it is customary to do a validation assessment. The validation of a (material) model functions as a reality-check, assessing whether the behaviour of the model is within the range occurring in-vivo. Ideally, such a validation would consist of a whole heart model, including the material model, and the comparison measures would consist of functional measures used in clinic, e.g. ejection fraction, end diastolic volume, stroke volume etc. As the scope of this thesis includes a SEM only, such validation was not possible. However, alternative reality-check cases were carried out by comparing computed results of the material model to results from mechanical tests done on cardiac tissue. Methods for the corresponding cases are discussed in Section 5.3.

5.1 MODEL DETAILS

The verification SEM that was used for all verification cases consisted of a simple cube with a length measure of 1x1x1 mm. Assigned node sets and surface definitions are depicted in Fig. 5.1. The verification model consisted of a 8-node linear hybrid brick single element (C3D8H). A local material orientation was assigned via the `*Orientation` keyword in the Abaqus .inp file. The local reference orientation was the same as the global orientation system. Either passive only or both passive and active material models were assigned to the model.

5.2 VERIFICATION TEST–CASES

Two kinds of test-cases were used to verify the passive and active components of the material model. Firstly, it was important to evoke the intended range of realistic operating conditions during the verification. For the passive component this was done with shear and equibiaxial test-cases, which were expected to show all characteristics of the material. The expected passive material characteristics were hyperelasticity, orthotropic behaviour during extension, isotropic behaviour under compression and incompressibility. For the active component an isometric contraction was carried out, where the FS-mechanism was expected to be seen. Computed out-
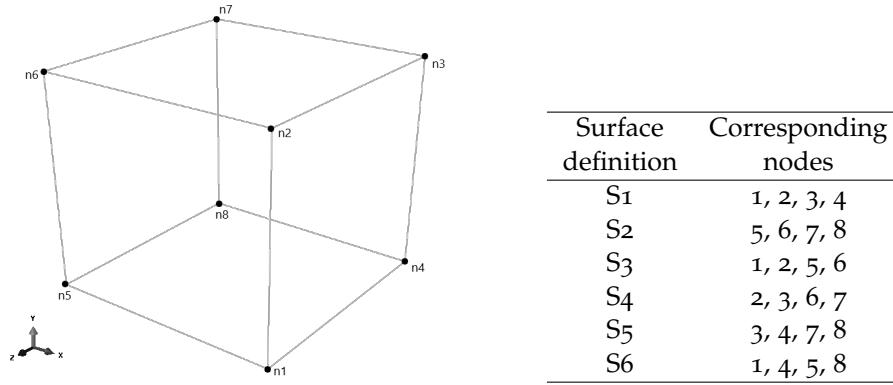
Figure 5.1: Node and surface sets of the single element model used in all verification cases.

comes were compared to both a benchmark model (UANISOHYPER_INV, [63]) and the analytical solution. The difference between the UMAT versus the UANISOHY-PER_INV and analytical solution were computed and assessed following requirements which are defined in Section 5.4.

Secondly, as mentioned in Chapter 4, implementation of a co-rotational coordinate system was challanging because in this case Abaqus passes a the abaqus local deformation gradient, instead of the classical co-rotational local form of the deformation gradient. To ensure correct implementation of the deformation gradient, a test-case consisting of a deformation in combination with a rigid body rotation [52] was carried out. Outcomes of the test-case done with a global coordinate system were compared to outcomes of the same test-case in local coordinate system. The stress- and strain-outcomes were expected to remain constant during rigid body rotation in the case where the local coordinate system was implemented. On the other hand, for the global case, the stress- and strain outcomes were expected to change during rigid body rotation. When both expectations were met, the deformation gradient was assumed to be well implemented in the UMAT. All test-cases are explained in detail in the following paragraphs.

5.2.1 Comparison of UMAT to Analytical and UANI Solutions

For the comparison of UMAT to the analytical solution and benchmark material model, a equibiaxial extension, equibiaxial compression, shear and isometric-contraction test-cases were carried out. The UMAT and benchmark UANI computation were done in Abaqus [6]. The analytical solutions were computed in Matlab [64]. The equibiaxial and shear test-cases were based on the paper of [8], which proposes an analytical solution for stresses and strains of the biaxial and simple-shear test-cases. These test-cases were done with only the passive component of the material model. The isometric-contraction test-case was based on [65], and included both passive and active material model components. In this section the computation of analytical solutions and the boundary conditions of mentioned test-cases are discussed.

Equibiaxial Extension and Compression Test-Cases

The equibiaxial extension test-case consisted of an extension deformation $u_e = 1.1$ of one plane, one plane with zero-displacement in its plane-normal direction and one plane that could move freely. For the equibiaxial compression test-case, two planes were assigned compression deformation $u_c = 0.9$, and one plane could move freely. The deformation gradient of the equibiaxial extension and compression test-cases had the form of Eq. 5.1, where corresponding λ_f, λ_s and λ_n values are defined in Table 5.2.

$$\mathbf{F} = \begin{bmatrix} \lambda_f & 0 & 0 \\ 0 & \lambda_s & 0 \\ 0 & 0 & \lambda_n \end{bmatrix} \tag{5.1}$$

Table 5.2: Boundary conditions of the equibiaxial extension and compression test-cases.

	λ_f	λ_s	λ_n
Extension C1	FM_e	u_e	u_e
Extension C2	u_e	FM_e	u_e
Extension C3	u_e	u_e	FM_e
Compression C1	FM_c	u_c	u_c
Compression C2	u_c	FM_c	u_c
Compression C3	u_c	u_c	FM_c

$u_e = 1.1$ and $u_c = 0.9$. FM is a plane with free movement.

Considering the incompressible assumption ($\lambda_f \cdot \lambda_s \cdot \lambda_n = 1$), the extension ratio of the free movement planes could be computed analytically by use of the following relation

$$FM_i = \frac{1}{(u_i)^2}, \qquad\qquad \text{where i = e, c.} \tag{5.2}$$

As for the computation of the stresses in the three orthogonal directions, the following equations applied [8]

$$\sigma_f = 2\psi_1(\lambda_f)^2 + 2\psi_{4f}(\lambda_f)^2 - p, \tag{5.3}$$

$$\sigma_s = 2\psi_1(\lambda_s)^2 + 2\psi_{4s}(\lambda_s)^2 - p, \tag{5.4}$$

$$\sigma_n = 2\psi_1(\lambda_n)^2 - p, \tag{5.5}$$

where the Lagrange multiplier p accounts for the incompressibility of the material. Considering the equibiaxial boundary conditions, there was one plane with free movement (i.e. no reaction force), therefore containing a stress value of zero. Because one of the three stress-values was taken as zero, there could be solved for p, shown by the following example where $\sigma_n = 0$

$$\sigma_n = 2\psi_1(\lambda_n)^2 - p = 0, \tag{5.6}$$

$$-p = -2\psi_1(\lambda_n)^2. \tag{5.7}$$

After substitution of p in the other equations, stresses in fibre and sheet direction were calculated by the following equations

$$\sigma_f = 2\psi_1 \cdot ((\lambda_f)^2 - (\lambda_n)^2) + 2\psi_{4f}(\lambda_f)^2, \tag{5.8}$$

$$\sigma_s = 2\psi_1 \cdot ((\lambda_s)^2 - (\lambda_n)^2) + 2\psi_{4s}(\lambda_s)^2. \tag{5.9}$$

Similarly, the same procedure was done for $\sigma_f = 0$, which resulted in the following equations for the stresses in sheet- and normal-direction

$$\sigma_s = 2\psi_1((\lambda_s)^2 - (\lambda_f)^2) + 2\psi_{4s}(\lambda_s)^2 - 2\psi_{4f}(\lambda_f)^2, \tag{5.10}$$

$$\sigma_n = 2\psi_1((\lambda_n)^2 - (\lambda_f)^2) - 2\psi_{4f}(\lambda_f)^2. \tag{5.11}$$

Lastly, it was done for $\sigma_s = 0$, resulting in the following equations

$$\sigma_f = 2\psi_1((\lambda_f)^2 - (\lambda_s)^2) + 2\psi_{4f}(\lambda_f)^2 - 2\psi_{4s}(\lambda_s)^2, \tag{5.12}$$

$$\sigma_n = 2\psi_1((\lambda_n)^2 - (\lambda_s)^2) - 2\psi_{4s}(\lambda_s)^2. \tag{5.13}$$

The equibiaxial extension and contraction cases were implemented in the SEM described above using the passive UMAT and the UANISOHYPER_INV in a local coordinate system. During all equibiaxial test-cases, three planes were assigned a zero-displacement in their plane-normal direction (Fig. 5.2). On the residual three planes, equibiaxial displacements following the deformation gradient Eq. 5.1 and Table 5.2 were applied. The planes indicated by FM had free movement (i.e. no deformation applied) in the Abaqus input file.
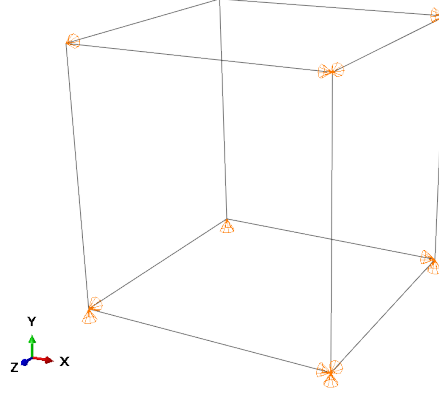

Figure 5.2: Basis boundary conditions of the equibiaxial test-cases showing the three planes which were assigned a zero-displacement boundary in their plane-normal direction.

Shear test-cases

For the shear test-cases, six simple-shear cases were considered with a shear of $\gamma = 0.5$. The deformation gradients of the shear in fs plane in f_0 and s_0 direction were taken as follows.

$$[\mathbf{F}] = \begin{bmatrix} 1 & \gamma & 0 \\ 0 & 1 & 0 \\ 0 & 0 & 1 \end{bmatrix} \quad \text{and} \quad [\mathbf{F}] = \begin{bmatrix} 1 & 0 & 0 \\ \gamma & 1 & 0 \\ 0 & 0 & 1 \end{bmatrix}. \tag{5.14}$$

For shear in sn plane, in s_0 and n_0 direction deformation gradients were taken as below.

$$[\mathbf{F}] = \begin{bmatrix} 1 & 0 & 0 \\ 0 & 1 & \gamma \\ 0 & 0 & 1 \end{bmatrix} \quad \text{and} \quad [\mathbf{F}] = \begin{bmatrix} 1 & 0 & 0 \\ 0 & 1 & 0 \\ 0 & \gamma & 1 \end{bmatrix}. \tag{5.15}$$

Similarly, for shear in fn plane, in f_0 and n_0 direction

$$[\mathbf{F}] = \begin{bmatrix} 1 & 0 & \gamma \\ 0 & 1 & 0 \\ 0 & 0 & 1 \end{bmatrix} \quad \text{and} \quad [\mathbf{F}] = \begin{bmatrix} 1 & 0 & 0 \\ 0 & 1 & 0 \\ \gamma & 0 & 1 \end{bmatrix}. \tag{5.16}$$

When applying these deformation gradients to Eq. 3.6, the analytical shear stress equations could be obtained. These can be written as follows

$$\sigma_{fs} = 2\gamma(\psi_1 + \psi_{4f}) + \psi_{8fs}, \tag{5.17}$$
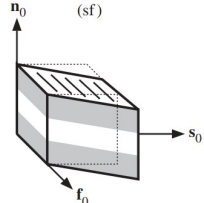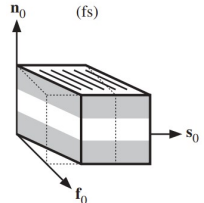$$\sigma_{fn} = 2\gamma(\psi_1 + \psi_{4f}), \tag{5.18}$$
$$\sigma_{sf} = 2\gamma(\psi_1 + \psi_{4s}) + \psi_{8fs}, \tag{5.19}$$
$$\sigma_{sn} = 2\gamma(\psi_1 + \psi_{4s}), \tag{5.20}$$
$$\sigma_{nf} = \sigma_{ns} = 2\gamma\psi_1. \tag{5.21}$$
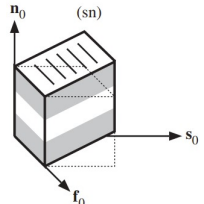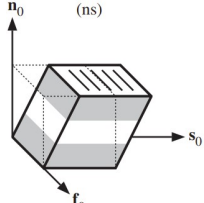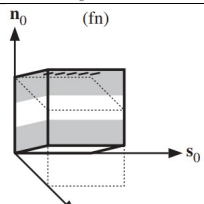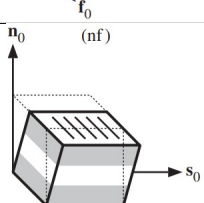
The boundary conditions corresponding to the shear deformation gradients for the use in the Abaqus input file are shown in Table 5.3. These were applied on the SEM described at the beginning of this section.

Table 5.3: Boundary conditions of the shear test-cases.

	Fix	Deformation	Figure
SF	S6 in X and Y S4 in Y S5 in Z	S4 in X	
FS	S1 in X and Y S2 in X S5 in Z	S2 in Y	
SN	S6 in Y and Z S4 in Y S2 in X	S4 in Z	
NS	S3 in Y and Z S2 in X S5 in Z	S5 in Y	
FN	S1 in X and Z S2 in X S6 in Y	S2 in Z	
NF	S3 in X and Z S5 in Z S6 in Y	S5 in X	

A shear of $\gamma = 0.5$ was implemented

Isometric–Contraction Test–Case

During the isometric-contraction test-case, the SEM was assigned a displacement corresponding to an extension ratio in fibre- and sheet-direction during a single contraction. Extensions of 0 to 40 % with increments of 10% were tested. The remaining planes were assigned zero displacement in their plane-normal direction. The active component of the stress in fibre and sheet direction were compared to the analytical solution.

5.2.2 Rotation Test–Cases

The rotation test-case consisted of four steps, where two steps contained solely passive behaviour, and two steps contained additional active behaviour (Table 5.4). The rotation test-case was carried out in a local coordinate system and a global coordinate system. For the global case the polar decomposition in the UMAT was removed resulting in a UMAT compatible to a global coordinate system. The global UMAT can be found in the supplementary material in Appendix A: "CARD-MAT/_for/UMAT_HO_TVE _GLOBAL.for". During the first two steps, the boundary conditions of the rotation test-case were based on deformation gradient $\mathbf{F_1}$

$$\mathbf{F}_1 = \begin{bmatrix} 1.10 & 0.00 & 0.00 \\ 0.00 & 1.20 & 0.00 \\ 0.00 & 0.00 & 0.75758 \end{bmatrix} . \tag{5.22}$$

For the last two steps, the SEM underwent a rigid body rotation based on rotation matrix $\mathbf{R}$, which resulted in deformation gradient $\mathbf{F_2}$

$$\mathbf{R} = \begin{bmatrix} cos(90) & -sin(90) & 0 \\ sin(90) & cos(90) & 0 \\ 0 & 0 & 1 \end{bmatrix} , \tag{5.23}$$

$$\mathbf{F}_2 = \mathbf{R} \cdot \mathbf{F}_1 . \tag{5.24}$$

All uneven steps were transition steps, consisting of 1 increment, while all even steps contained a contraction and consisted of 100 increments. To implement matrices $\mathbf{F_1}$ and $\mathbf{F_2}$, the coordinates of all nodes were defined. This was incompatible with the hybrid element and incompressibility user subroutine formulation that was used in the designed material model, as it creates an over-constraint. Therefore, for this test-case only, a C3D8 element was used without incompressibility definition. This decision is considered reasonable, as this test-case does not verify the incompressibility of the material model.

Table 5.4: An overview of the steps of the rotation test-cases.

	Step 1	Step 2	Step 3	Step 4
Boundary conditions	$\mathbf{F}_0 \rightarrow \mathbf{F}_1$	$\mathbf{F}_1$*	$\mathbf{F}_1 \rightarrow \mathbf{F}_2$	$\mathbf{F}_2$*

* In this step a contraction takes place.
$\mathbf{F}_0$ depicting the undeformed state of the SEM.

5.3 REALITY–CHECK TEST–CASES

A reality-check would ideally compare the computed data to in-vivo measured data. However, for passive and active myocardial mechanical behaviour, this data is not available in the literature to my best knowledge. Comparing the computed data to in-vitro experiments is a good alternative, and is discussed further in section 5.3.1. The used models and test-cases were designed to be similar to the experiments done to obtain the experimental data, which are discussed in section 5.3.1.

5.3.1 Experimental Datasets

Related work on the subject of mechanical tests done on myocardium has a relatively short history. Early data consists of uniaxial testing on papillary muscles, e.g. [66], [67]. When evidence was found that the myocardium was anisotropic, the more complex biaxial and shear tests on ventricular myocardium specimens were carried out. Earlier contributions were biaxial tests, documented by Demer et al. [68] and Yin et al. [69] which use similar experimental testing apparatus. However, the specimen preparation did not ensure total deactivation of myocardium contraction. Novak et al. [70] used the same experimental setup but contrary to Demer et al. [68] and Yin et al. [69] used an oxygenated cardioplegic solution to ensure total passive behaviour of the samples. Smaill et al. [71] came up with a new apparatus claiming that the specimens could be mounted more quickly, and relatively small samples could be tested. Additionally, they perfused the specimen in a cardioplegic solution to ensure passivity of the myocardium. Dokos et al. [23] were the first who did shear tests on cubic pig heart samples. Most recent data comes from Sommer et al. [24], who were the first to do mechanical tests – biaxial and shear – on human cardiac specimens.

From available experimental data, results of biaxial tensile tests of Sommer et al. [24] and triaxial shear tests of Dokos et al. [23] shall be included as reference for the passive cases. Note that the shear data of Sommer et al. [24] is used to optimize the material parameters of the Holzapfel Ogden material model. Finally, for the assessment of the active material model, results of the isotonic contraction tests of Holubarsch et al. [72] were used.

Reality–Check Model Details

All Abaqus models used for the reality-check cases were similar to the verification SEM. The only differences were the dimensions, which are shown in Table 5.5.

Reality–Check Test–Cases

As mentioned in the section 5.3.1, test-cases were based on mechanical experiments done on cardiac tissue. The first set of reality-check test-cases consisted of 'true' planar biaxial test-cases. These test-cases were done by assigning planar biaxial stretches with different extension ratios (F:S = 1:0.5, 0.5:1). The test-cases assessed the occurrence of direction-dependent nonlinear material response. The second set of reality-check test-cases consisted of the shear test-cases. These involved six types of shear displacements (SF, NF, FS, NS, FN and SN), where a maximal shear displacement of 50% was assigned to a cube SEM with a length measure of 3 x 3 x 3 mm.

Experimental isotonic contraction test-cases of Holubarsch et al. [72] were done on 8 healthy human heart specimens (left ventricle), and 48 specimens of explanted hearts (end stage chronic heart-failure). For the SEM in this test-case, a length measure of 4.9x0.24x0.24 mm was used. In the first step an extension was carried out

by putting negative pressure of 0.0068 MPa in f-dir, and 0.00068 MPa in s- and n-dir. The extension step was followed by a step containing a contraction. The T_{max} was optimised to have a similar peak as was presented in the experimental data of Holubarsch et al. [72].

Table 5.5: Methods of the different validation test-cases done on a SEM.

	Mat. model	Modelling features		Validation	
	A/P	Geometry	Max. extension [%] or max. load [MPa]	Ref.	Species and sample size
Biaxial tensile	P	5 x 5 x 2.3 mm	20 %	[24]	human (n = 26)
Triaxial shear	P	3 x 3 x 3 mm	50 %	[23]	porcine (n = 6)
Isotonic contraction	P+A	4.92 x 0.24 x 0.24 mm	0.0068 MPa + contraction*	[72]	human (n = 48)

P = passive, A = Active. *Contraction with Tmax = 0.0096 MPa.

5.4 VERIFICATION REQUIREMENTS

For all verification test-cases a maximum error of 1% of the relevant output parameter was adhered to as requirement. Additionally, the reality-check test-cases were compared in a qualitative manner i.e. looking at occurring phenomenon and value trends.

A measure derived from the mean absolute percentage error (MAPE) was used for the error calculation. MAPE is a much used measure of prediction. However, a down-side of this measure occurs when the actual value gets zero or close to zero. In this situation the error becomes unrealistically high, or even infinite. To mitigate this problem, the error was normalised w.r.t. the maximal actual value instead of normalising over the actual value at the corresponding time-point. This results in the MAPE_{max}, which was used in this thesis for error calculation. MAPE and MAPE_{max} were defined as follows

$$\text{MAPE} = \frac{100}{N \cdot I} \sum_{n=1}^{N} \sum_{i=1}^{I} \left| \frac{A_{n,i} - F_{n,i}}{A_{n,i}} \right|, \tag{5.25}$$

$$\text{MAPE}_{max} = \frac{100}{N \cdot I} \sum_{n=1}^{N} \sum_{i=1}^{I} \left| \frac{F_{n,i} - A_{n,i}}{A_{max}} \right|, \tag{5.26}$$

where F is the forecast value, A is the actual value, N is the number of nodes and I is the number of increments. In some cases it was considered interesting to present the error as a function of e.g. the time. In these cases, the absolute percentage error normalised w.r.t. the maximal actual value (APE_{max}) value was used, defined as

$$\text{APE}_{max} = \frac{100}{N} \sum_{n=1}^{N} \left| \frac{F_n - A_n}{A_{max}} \right|. \tag{5.27}$$

6 | VERIFICATION RESULTS AND DISCUSSION

6.1 COMPARISON OF UMAT TO ANALYTICAL AND UANI SOLUTIONS

6.1.1 Equibiaxial Test–Cases

Fig. 6.1 and 6.2 show graphs of the analytical solution and the Cauchy stress values computed by UMAT and UANI as a function of the nominal strains ($E_{ii}^N = \sqrt{C_{ii}} - 1$, where ii = 11, 22, 33). From the graphs showing an orientation where an extension was applied (Fig. 6.1 b, c, d, f, g, h), it is visible that the same strain value in all three orthotropic directions results in different peak-stresses. This observation shows that the material behaved in an orthotropic manner when it was extended. On the other hand, when looking at the individual equibiaxial compression test-cases, the graphs that show compression of the SEM (Fig. 6.2 b, c, d, f, g, h) show similar peak-stress results for the same strain-value. This is evidence of the isotropic behaviour in compression. Also, hyperelasticity is clearly visible in the graphs showing extension and compression.

Some differences between the UMAT results and the analytical solutions were visible, predominantly in the orientations where free movement was allowed. However, relative to the maximal stress and strain value of that case, these difference were considerably small. The mentioned differences are quantified in Table 6.1 and Table 6.2. For the equibiaxial extension and compression tests the UMAT complied with the set verification requirement, as the tables show no values bigger than 1%.

Table 6.1: Quantification of the error ($\mathrm{MAPE}_{max}[\%]$) of UMAT relative to either the analytical solution or the UANI results of equibiaxial extension test-cases.

	Extension C1		Extension C2		Extension C3	
vs. analytical	$MM(\sigma)$	$MM(E)$	$MM(\sigma)$	$MM(E)$	$MM(\sigma)$	$MM(E)$
F-dir	3.916E-05	1.115E-07	1.742E-04	1.923E-05	1.329E-05	1.923E-05
S-dir	4.030E-05	1.923E-05	1.742E-04	1.115E-07	1.389E-05	1.923E-05
N-dir	3.972E-05	1.923E-05	1.743E-04	1.923E-05	1.396E-05	1.115E-07
vs. UANI						
F-dir	1.738E-05	9.148E-06	1.798E-05	1.896E-05	1.767E-05	1.896E-05
S-dir	1.711E-04	1.896E-05	1.717E-04	9.327E-06	1.715E-04	1.896E-05
N-dir	1.050E-05	1.896E-05	9.336E-06	1.896E-05	9.255E-06	9.327E-06

$MAPE_{max}$ *stress and strain error values are abbreviated to $MM(\sigma)$ and $MM(E)$.*

Table 6.2: Quantification of the error (MAPE_{max}[%]) of UMAT relative to either the analytical solution or the UANI results of equibiaxial compression test-cases.

	Compression C1		Compression C2		Compression C3	
vs. analytical	$MM(\sigma)$	$MM(E)$	$MM(\sigma)$	$MM(E)$	$MM(\sigma)$	$MM(E)$
F-dir	1.405E-04	1.006E-05	1.653E-04	6.825E-06	1.834E-04	6.825E-06
S-dir	1.409E-04	6.825E-06	1.688E-04	1.006E-05	1.835E-04	6.825E-06
N-dir	1.409E-04	6.825E-06	1.653E-04	6.825E-06	1.836E-04	1.006E-05
vs. UANI						
F-dir	2.790E-04	9.888E-06	2.792E-04	6.923E-06	2.792E-04	6.920E-06
S-dir	2.756E-04	6.920E-06	2.788E-04	9.888E-06	2.756E-04	6.920E-06
N-dir	2.756E-04	6.920E-06	2.788E-04	9.888E-06	2.756E-04	6.920E-06

MAPE_{max} *stress and strain error values are abbreviated to $MM(\sigma)$ and $MM(E)$.*

6.1.2 Shear Test–Cases

Fig. 6.3 shows graphs of the analytical solution and the Cauchy shear stress values computed by UMAT and UANI as a function of the shear strain. Firstly, orthotropic material behaviour could be established by considering the peak-shear-stress values, which all showed different values. Note that the peak-shear-stresses all occurred at the same strains. Strain-stiffening was visible, which is an indication of hyperelasticity.

Fig. 6.4 shows the difference in shear stress results computed by the UMAT compared to results computed by the UANI and the analytical solution. This is quantified by the absolute percentage error ($\text{APE})_{max}$ value, which was shown as a function of the shear strain. The APE_{max} values compared to the UANI results showed much similarity, with a maximal APE_{max} of 1.16E-5 % (Table 6.3). However, the APE_{max} compared to the analytical solution showed more discrepancies with a maximal APE_{max} error of 16.97% in the FN direction. Only the NF and NS cases complied with the set verification requirement of 1%, all other cases displayed higher error values (Table 6.3).

The higher errors occurring when comparing the UMAT results with the analytical solution could have multiple causes. The first (most obvious) reason could be the incorrect application of the HO model in the UMAT. However, this was deemed unlikely as the UANI and UMAT showed very similar results as shown by the low APE_{max} error values. Secondly, and more likely, the discrepancy could be caused by one of multiple numerical formulations used, i.e. the Newton-Rhapson method, used by Abaqus, or the numerical method used for computing the elasticity tensor.

Table 6.3: Maximal APE_{max}[%] values of Fig. 6.4, comparing computed UMAT values with the analytical or UANI computed solution.

max. APE_{max}[%]	SF	FS	SN	FN	NF, NS
UMAT vs. Analytical	2.278	15.52	3.368	16.97	0.2557
UMAT vs. UANI	9.61E-06	6.94E-06	1.16E-05	3.07E-06	8.71E-06

6.1.3 Isometric Contraction Test–Cases

In Fig. 6.5 the active part of the stresses of the isometric contraction test-cases with strains of 0 to 0.4, with increments of 0.1, are displayed as a function of time from the beginning of the action potential. Note that the higher the applied strain, the higher the resulting peak-stress value, which implies occurrence of the FS-mechanism in the UMAT. For the isometric contraction test-cases, the UMAT complied with the set verification requirement, as the MAPE_{max} error values shown in Table 6.4 were all smaller than 1%.

Table 6.4: MAPE_{max} [%] errors of the isometric contraction test-cases, under various stretches.

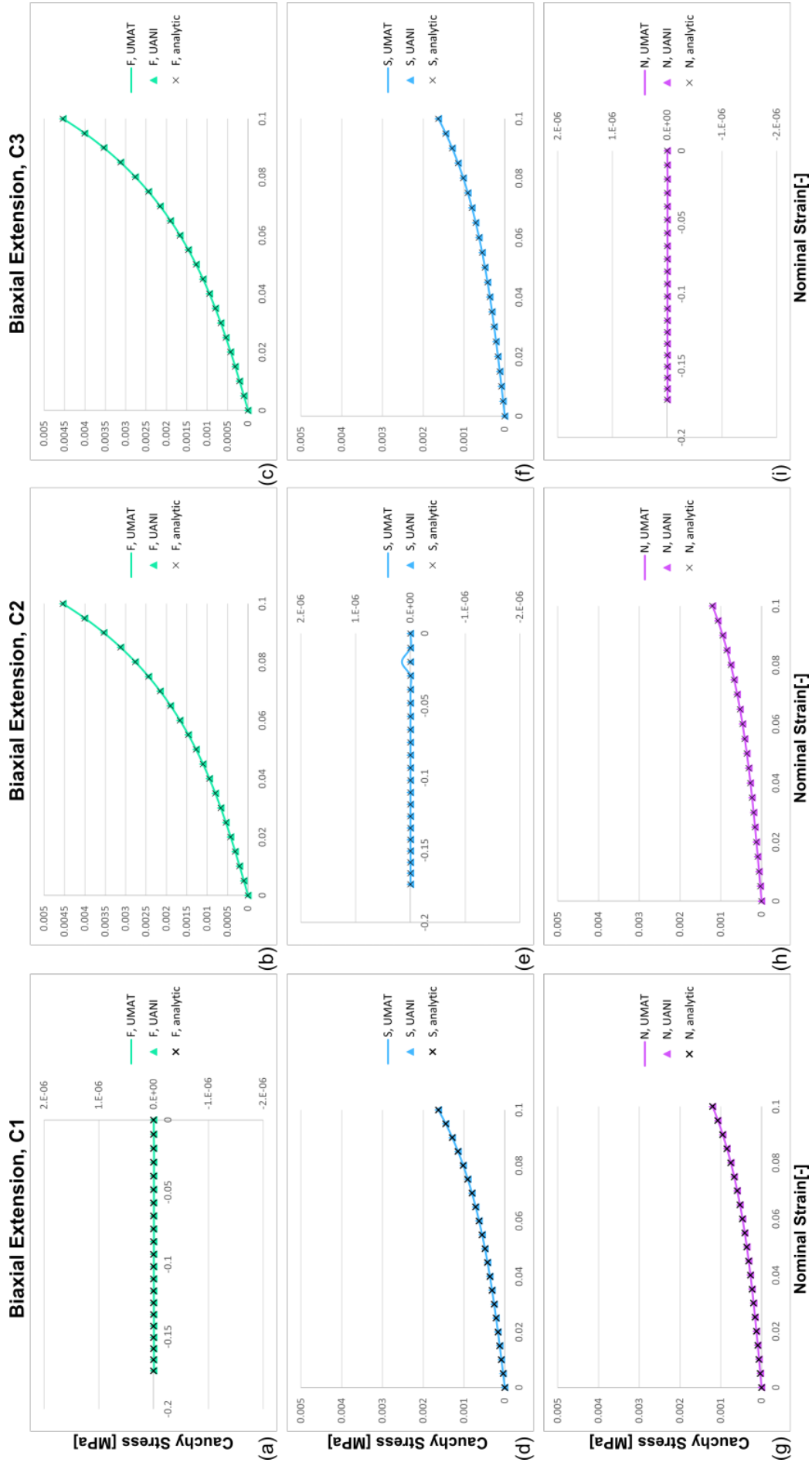|	Stretch 0.0	Stretch 0.1	Stretch 0.2	Stretch 0.3	Stretch 0.4
UMAT vs. analytical	3.66E-07	5.10E-07	5.98E-07	6.43E-07	8.18E-07

Figure 6.1: Stress and strain results of the equibiaxial extension test-cases in fibre, sheet and normal directions (in the top, middle and bottom rows, respectively) as computed analytically and by the UMAT and UANISOHYPER_INV (UANI) passive material models. Boundary conditions of case 1 consist of: λ_f has free movement, $\lambda_s = 1.1$ and $\lambda_n = 1.0$. For case 2 they consist of $\lambda_f = 1.1$, λ_s has free moment and $\lambda_n = 1.0$. For case 3 it consists of $\lambda_f = 1.1$, $\lambda_s = 1.0$ and λ_n has free movement. MAPE$_{max}$ error values are quantified in Table 6.1
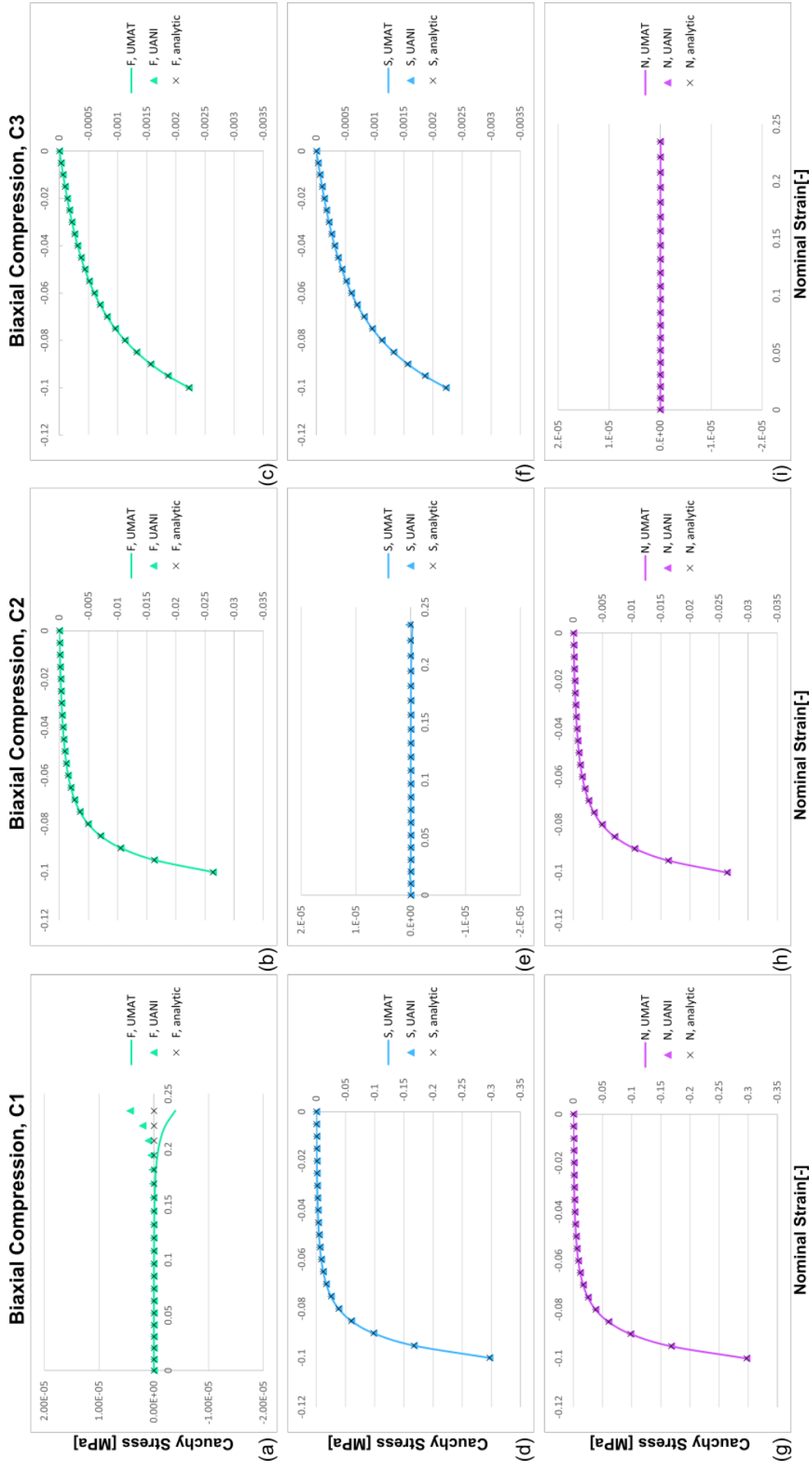
Figure 6.2: Stress and strain results of the equibiaxial compression test-cases in fibre, sheet and normal directions (in the top, middle and bottom rows, respectively) as computed analytically and by the UMAT and UANISOHYPER_INV (UANI) passive material models. Boundary conditions of case 1 consist of: λ_f has free movement, $\lambda_s = 0.9$ and $\lambda_n = 1.0$. For case 2 they consist of $\lambda_f = 0.9$, λ_s has free moment and $\lambda_n = 1.0$. For case 3 it consists of $\lambda_f = 0.9$, $\lambda_s = 1.0$ and λ_n has free movement. MAPE$_{max}$ error values are quantified in Table 6.2.
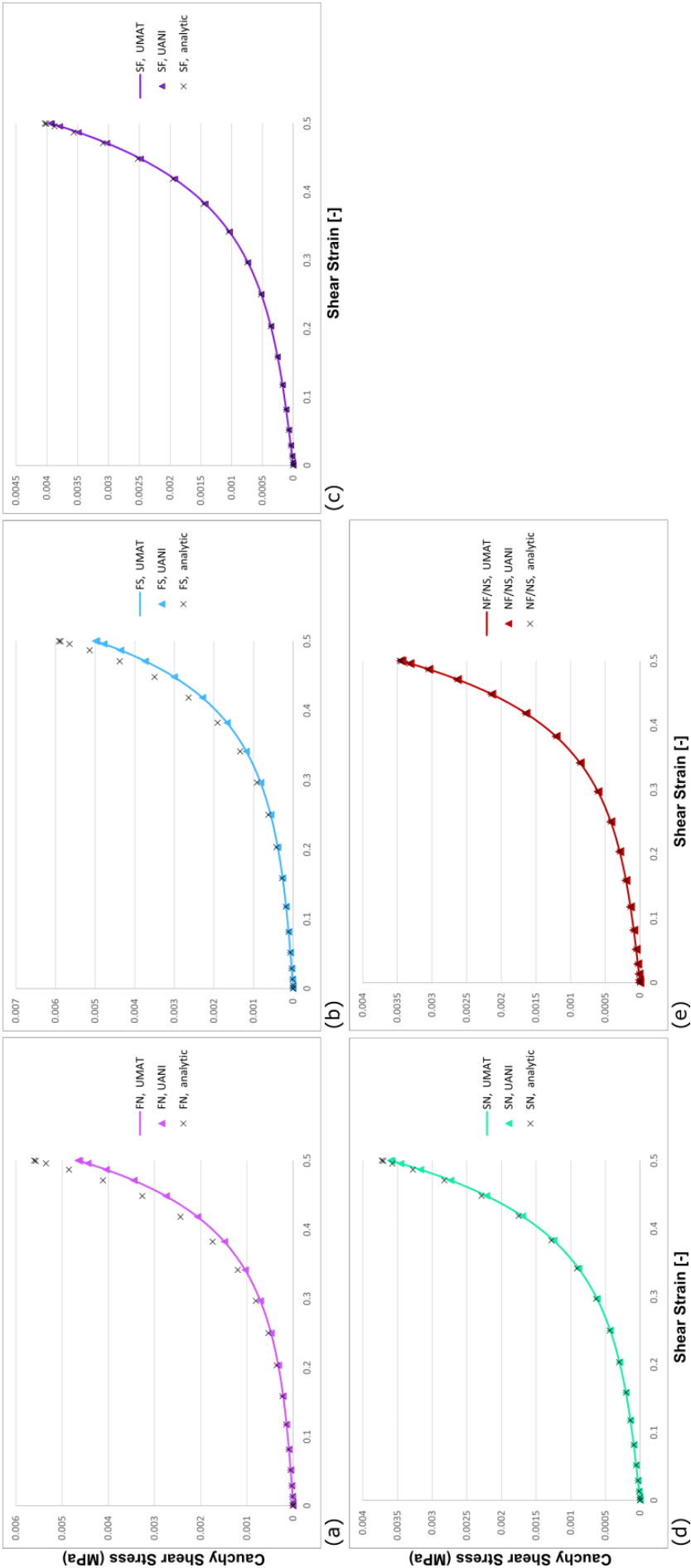
Figure 6.3: Shear stress and shear strain results of the shear test-cases as computed analytically and by the UMAT and UANISOHYPER_INV (UANI) passive material models. FN and NF cases show σ_{13}, SN and NS cases show σ_{23} and SF and FS cases show σ_{12} shear stress values. The boundary conditions are presented in Table 5.3. APE_{max} error values are quantified in Fig. 6.4.
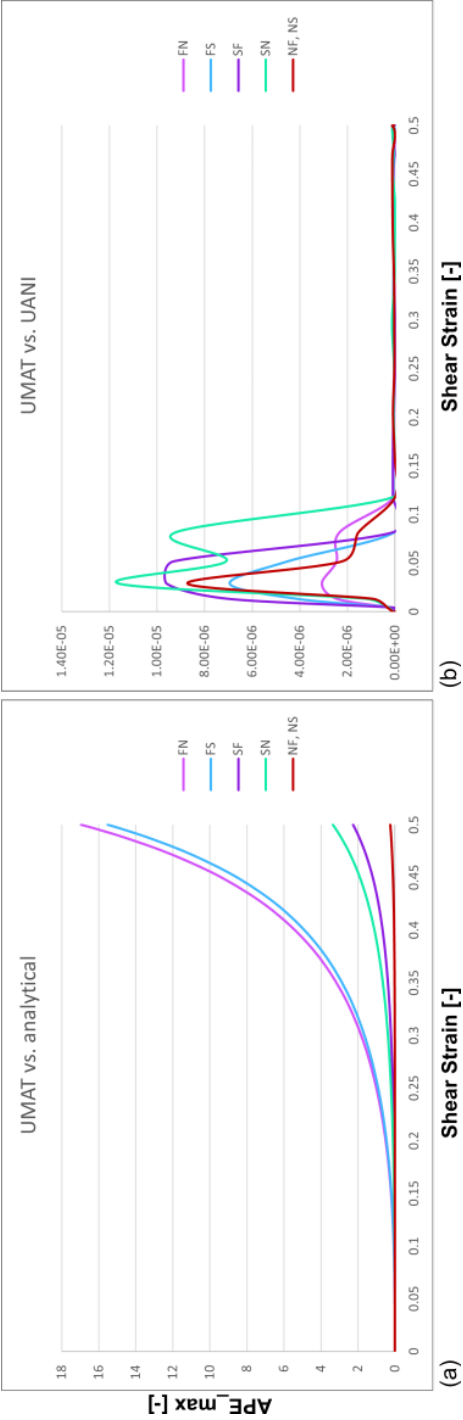
Figure 6.4: APE_{max} error values of the (a) UMAT vs. analytical and (b) UMAT vs. UANISOHYPER_INV (UANI) results of Fig. 6.3.

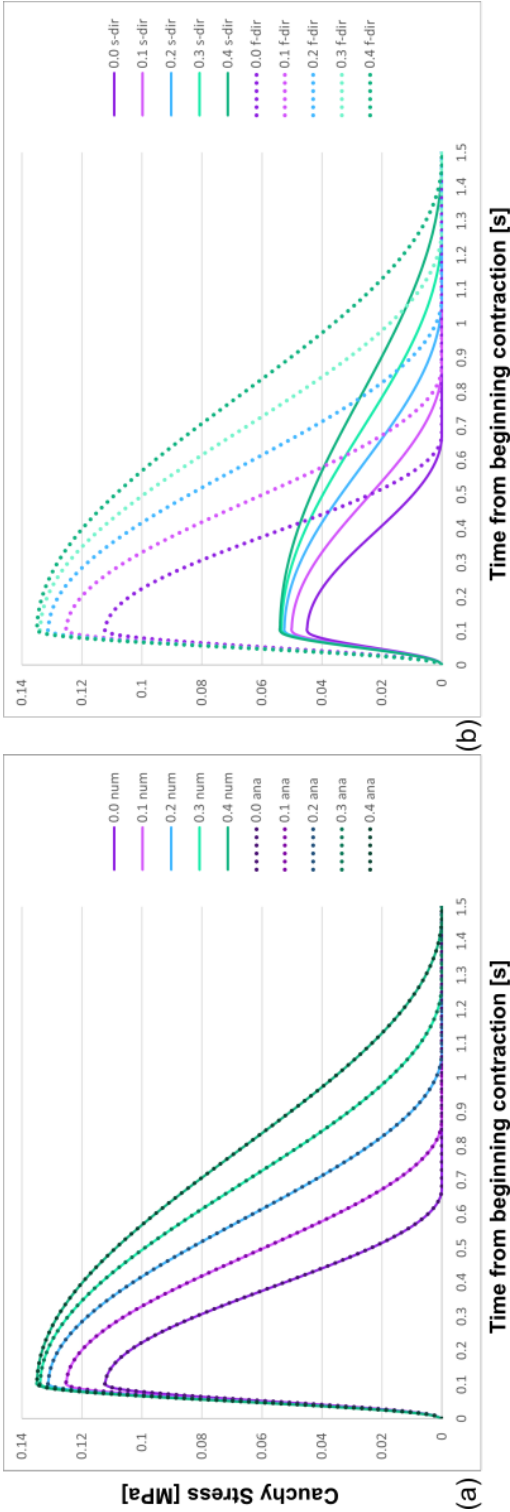Figure 6.5: Results of the isometric contraction test-cases with the following stretches; 0.0, 0.1, 0.2, 0.3 and 0.4. (a) Analytical- and UMAT-computed results of the active stresses in fibre-direction. (b) Active stresses in fibre- and sheet-directions as computed by UMAT. MAPE$_{max}$ error values are quantified in Table 6.4. (b) Active stresses in fibre- and sheet-directions as computed by UMAT.

6.2 ROTATION TEST-CASES

The verification of the application of deformation gradient in UMAT was done by the rotation test-cases, where a biaxial extension was performed in combination with a rigid body rotation in both a global and co-rotational local coordinate system. Fig. 6.6 shows the SEM including a global coordinate system compatible UMAT and a local coordinate system compatible UMAT (the latter including an `*Orientation` keyword in the Abaqus .inp file). Note that for the stretch step, the global, local reference and local current basis systems were all the same. However, after rotation, the local current basis system has rotated with the SEM, while the other two basis systems remains in their initial position. Consequently, the σ_{11} stress value in the global coordinate system changed value, while this value remained constant in the local coordinate system as the basis system co-rotated with the rigid body deformation.
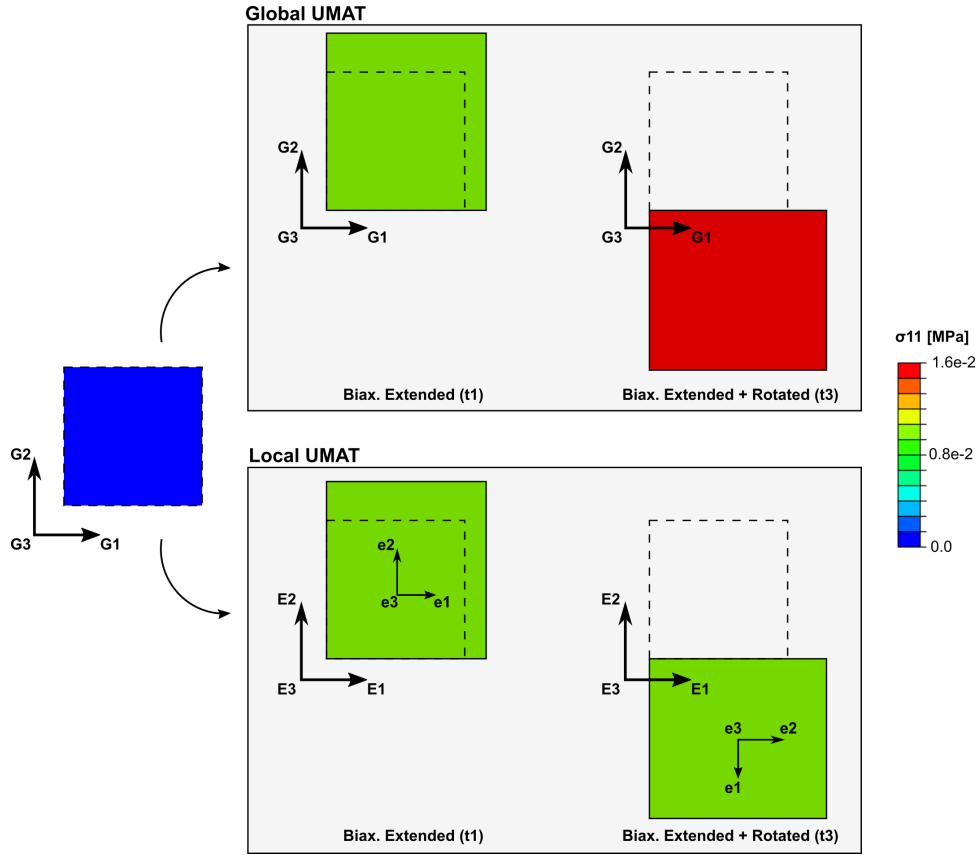

Figure 6.6: Passive stresses in fibre direction (σ_{11}) at timepoint $t1$ (biaxially extended configuration) and $t3$ (biaxially extended and rotated configuration) of Fig. 6.7 projected on the SEM in various configurations. The upper SEMs include the global UMAT, while the lower SEMs include the local UMAT. Global, local reference and local current basis systems are visualised by G_i, E_i and e_i, respectively, where $i = 1, 2, 3$.

Fig. 6.7 shows the transient stresses of the UMAT in global and local configuration during all four steps of the test-case. In Fig. 6.7 (a) and (c) the passive stresses are presented (these graphs correspond to Fig. 6.6). The stresses computed with the UMAT in global configuration changed after the rigid body rotation, while in the local configuration the stresses remained constant. Similarly, the active stresses presented in Fig. 6.7 (b) and (d), show changes in the peak force of the contraction after rigid body rotation in the global configuration, while the peak force remained constant in the local configuration. This verifies the correct application of the deformation tensor in both active and passive material models in the UMAT.
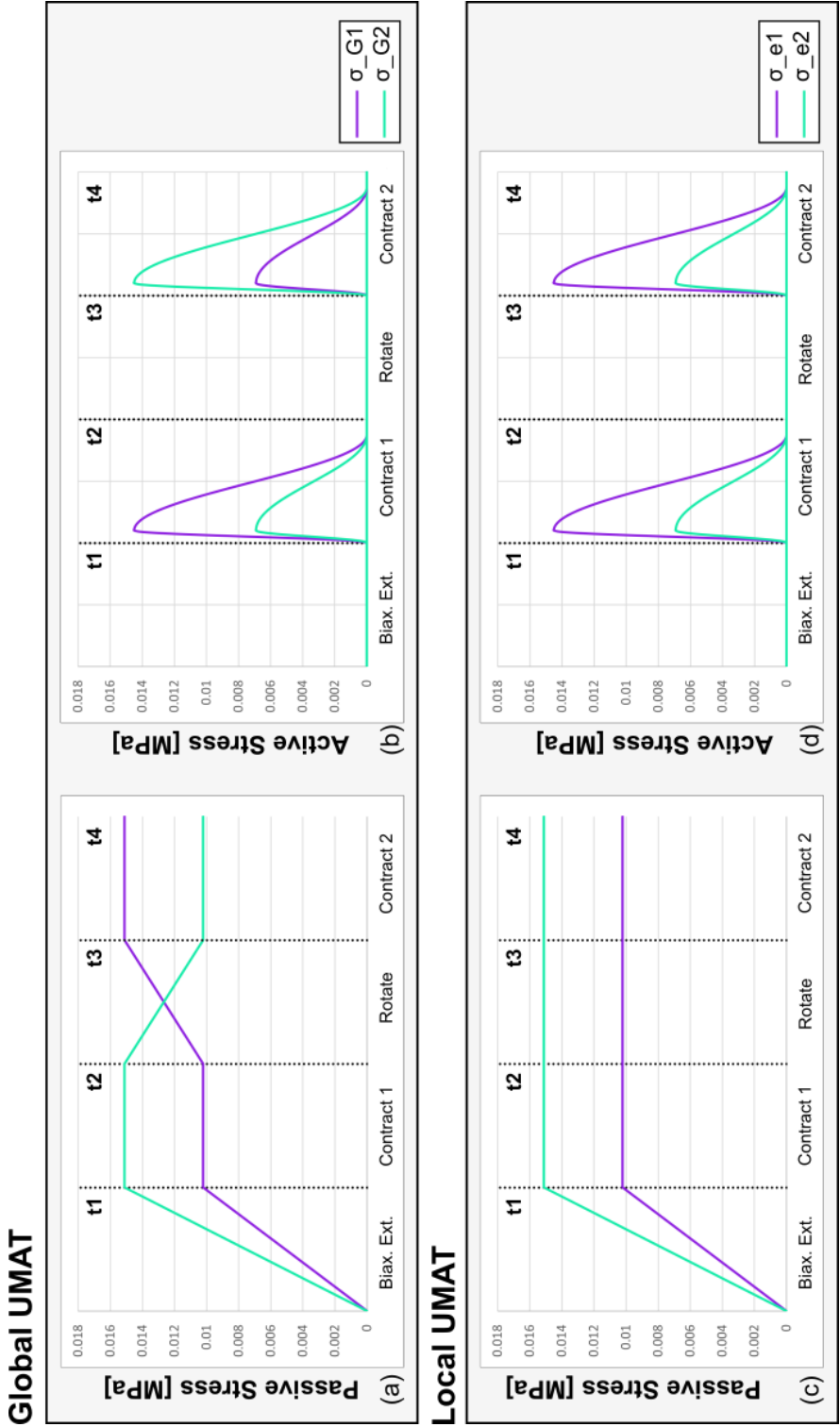
Figure 6.7: Active and passive stress results from the rotation test-cases in global (G_i) and local (e_i) configuration were plotted against the different steps of the rotation test-cases, where $i = 1, 2$. The last increment of each step were assigned a corresponding time-point, $t_1 - t_4$. Graph (a) and (c) show the passive part of the stresses. Graph (b) and (d) show the active part of the stresses. Biax. Ext. = Biaxial Extension

6.3 REALITY–CHECK TEST–CASES

6.3.1 Biaxial Extension Test-Case

In Fig. 6.8, the Cauchy stress values of the biaxial extension test-cases with FS-extension ratios of 0.5:1 and 1:0.5 are shown as a function of the strain. Both computed values of the UMAT and experimental data ([24]) are shown. Firstly, the stress-strain curve of the computed UMAT and experimental data in F-direction were quite similar. However, in the S-direction the computed UMAT results showed gradually more difference w.r.t. the experimental data as the strain increased. Secondly, in both the experimentally obtained and UMAT computed stress-strain curves, strain-stiffening was visible, indicating hyperelasticity. Also, considering that the maximal strain values are the same in all test-cases, the peak-stress values showed variable magnitudes. As this test-case consists of biaxial extension, no information about the normal-direction was provided by the experimental data and the results of the UMAT. Therefore, this data can not show orthogonality of the material, but it does show transversely-isotropic behaviour. Lastly, the hysteresis behaviour of the experimental data stands out, possibly indicating viscoelasticity. Viscoelasticity was not included in the UMAT material model.

6.3.2 Shear Test-Case

In Fig. 6.9, stress-strain curves resulting from shear tests of Dokos et al. [23] and Sommer et al. [24] and the computed UMAT results are shown. When looking at the qualitative aspect of the stress-strain curves, the UMAT was in the range of the experimental data as all curves are showing strain-stiffening and orthotropic behaviour. Only the hysteresis behaviour of the experimental data, possibly indicating viscoelasticity, was not represented by the computed UMAT results. When assessing the peak-stresses in general, the UMAT results and the experimental data showed the same trend. However, when looking in more detail, during the FS and FN cases the computed stress-peak results of the UMAT and experimental data of Sommer et al. [24] were lower than the experimental data of [23]. On the other hand, during the NF and NS cases the peak-stress results of the UMAT were higher than all experimental data results. Note that the shear data of [24] was used for optimisation of the parameters, which were applied in the passive HO model.
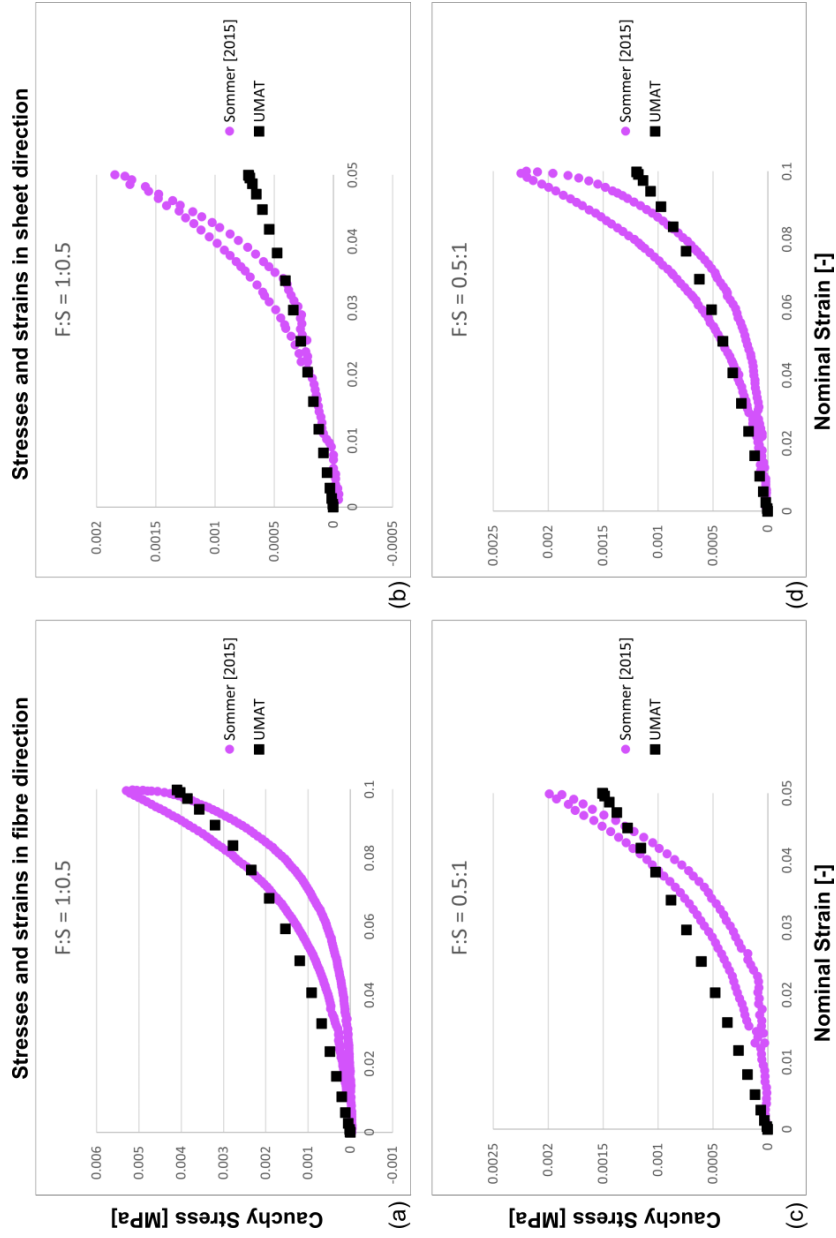
Figure 6.8: Stress-strain results during biaxial extension test-case of the UMAT versus experimental data extracted from fig 7d. of [24]
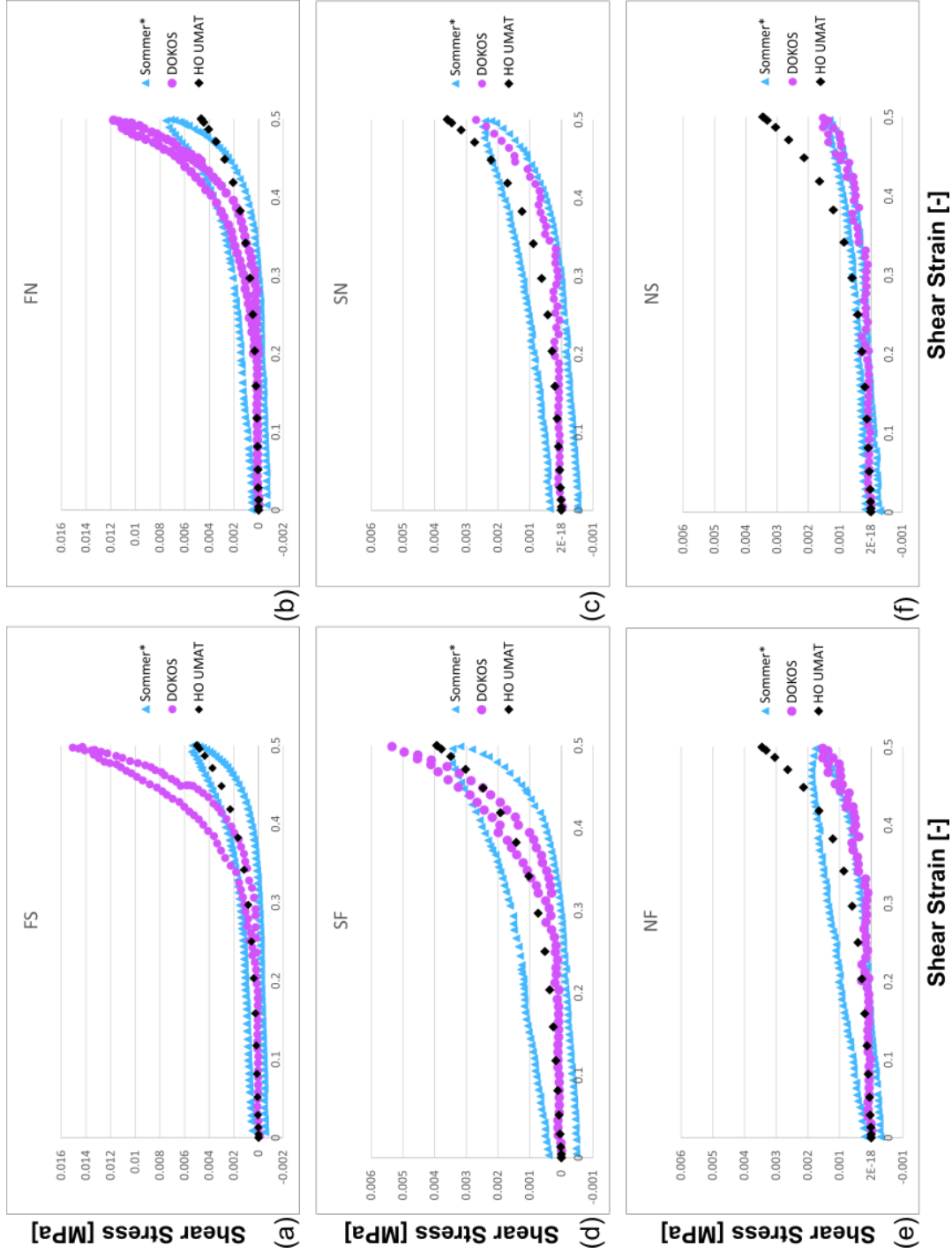
Figure 6.9: Stress-strain results of the UMAT versus experimental data extracted from Fig. 11 of Sommer et al [2015] and Fig. 6 of Dokos [2002]. The latter information is slightly adapted: fs and fn information is switched around as compared to the figure in Dokos [2002], as the data is inconsistent with the rest of the data presented in the article (as explained in Holzapfel and Ogden [2009]). The shear data of Sommer et al. [2015] was used for the optimization of the material parameters, and therefore was not considered for the validation error calculation. However, it was added as additional information.

6.3.3 Isotonic–Contraction Test–Case

In Fig. 6.10 the transient length of a (single-element) specimen during isotonic contraction is plotted against the time from the beginning of the contraction. Both results of the UMAT and results of the experiments of [72] are shown. The behaviour of the UMAT and the experimental data showed a similar trend. However, some differences occured. Firstly, the peak-deformation of the contraction computed by the UMAT was earlier than the experimental data. Secondly, the relaxation of the UMAT was slower than that of the experimental data.
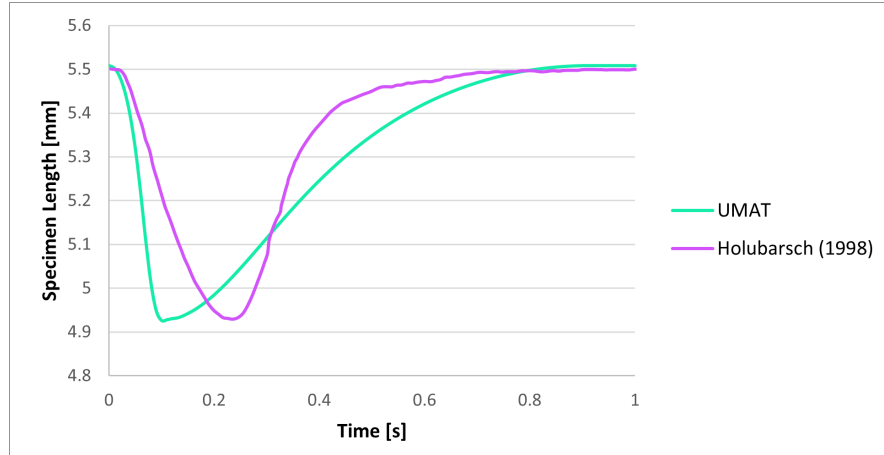

Figure 6.10: Results of the isotonic contraction test-case computed by the UMAT and experimental data based on isotonic tests done on LV rat papillary muscles. Data presented here is extracted from Fig. 1B of [72]. A T_{max} of 0.0096 is used.

7 | GENERAL DISCUSSION AND CONCLUSIONS

7.1 COMPARISON TO THE FIELD

Current trends in cardiac FE modelling aim to develop patient-specific medical treatment, improve efficiency of clinical trials of medical devices and give more insight in the physiology and pathology of cardiac diseases. Computational material models are essential for cardiac FE modelling. However, no material model suited for active heart tissue modelling is available in commercial available FE software. Consequently, researchers are forced to implement the material models by themselves via e.g. a user subroutine. Implementation of a user subroutine is complex as it necessitates thorough knowledge of continuum mechanics and tensor algebra. Additionally, available FE software manuals, research papers and books provide information containing only limited details. Therefore, it is a time-consuming undertaking, which is prone to errors. This thesis provides a detailed description of the implementation of a material model approximating the passive and active behaviour of cardiac tissue using the user-defined material subroutine UMAT in commercially available FE software Abaqus. Passive cardiac tissue behaviour was modelled by the nonlinear, hyperelastic, orthotropic, incompressible, invariant-based [8] model. Active cardiac tissue behaviour was implemented by the Time-Varying Elastance (TVE) model [9]. The models were combined via the active stress approach and were implemented in Abaqus via the user subroutine UMAT in a local coordinate system with a numerically computed elasticity tensor.

Verification of the implemented material models showed good agreement with the analytical solution of equibiaxial extension and equibiaxial compression test-cases, as all test-cases showed an MAPE$_{max}$ or APE$_{max}$ error lower than 1%. Shear test-case results of the UMAT showed some bigger APE$_{max}$ values w.r.t. the analytical solution (maximal 16%), possibly caused by numerical errors during the elasticity tensor computation. Results of the reality-check cases showed similar trends to the mechanical experiments done on cardiac tissue on which these cases are based.

This thesis extends the knowledge provided in the articles of [52], [61] and 'The Hitchhikers Guide to ABAQUS' of [62]. These articles provide a basis-knowledge for the implementation of a SEF in the user subroutine UMAT that is used in a local coordinate system, of which [61] describe the implementation of the Holzapfel-Gasser-Ogden material model in the user subroutines UANISOHYPER_INV and UMAT. Additionally, [52] provides a step-by-step description of the different forms of the deformation gradient as used by Abaqus, especially when implementing either a local or global coordinate system. Lastly, the paper of [62] provides practical tips and tricks for the development of a user subroutine. This thesis combines and extends this information by applying it to the case of the combined passive HO and active TVE model. Although used before in e.g. [32], [65], this is the first time that the combined HO and TVE model implemented in a UMAT is reproducible by making it publicly available.

Although commercially available FE software do not contain built-in active material models, they do contain built-in passive material models that are suited for modelling biological tissues, e.g. the Holzapfel-Gasser-Ogden model available in

Abaqus/CAE as the Holzapfel model [73]. With only a passive material model it is possible to model the end-systolic and end-diastolic volumes, as well as the pressure during the ventricular filling phase (Fig. 2.2). Addition of the active material model enables the computation of transient pressures during the complete systole and isovolumetric relaxation.

7.2 LIMITATIONS AND ASSUMPTIONS

The limitations of the proposed UMAT including the combined HO and TVE model need to be discussed. First of all, the proposed UMAT assumes incompressibility. This assumption is frequently made for biological tissues, because the amount of water in biological tissue is high [19]. However, [21] shows that in particular during the systole, significant volume changes occur in cardiac tissue. Therefore, the incompressibility assumption is be outdated. However, because of simplicity reasons, incompressibility is still used in this thesis. A second limitation is the omission of viscoelasticity. During experimental tests, cardiac tissue shows hysteresis, for example the experimental data of Dokos et al. [23] and Sommer et al. [24] presented in Fig. 6.8 and Fig. 6.9. The hysteresis can be most probably attributed to viscosity. However, as currently no appropriate viscoelastic orthotropic material model exists, it was outside the scope of this thesis to add viscosity to the current model. Lastly, the current model is based on material parameters taken from literature, while the model is meant to be patient-specific. Although it is not done during this thesis, it is possible to optimise the model with patient-specific data. This can be done with for example minimal square optimisation based on clinical parameters like ventricular pressure and volume, as is done for both the HO and TVE material parameters in [42] on a whole heart FE-model.

Concerning the material model implementation in the UMAT, limitations include the following. Firstly, currently the model can only produce one contraction per job (computer-run). Additionally, to ensure an accurate timing of the contraction, UMAT material parameter dt must correspond to the fixed increment size of the step in which the contraction takes place. Consequently, automatic time incrementation cannot be used during this step.

The results of the reality-check cases give insight into the realism of the model. However, due to heterogeneity between experimental setups of different papers, direct comparison between the UMAT and experimental data was not possible, only result-trends could be compared. An example of this is presented in Fig. 6.9 where the results of experiments done by Dokos et al. [23] and Sommer et al. [24] showed different values. While the loading strain values of the two experiments were the same, some important differences were found (Table 7.1). Although it was not tested in this thesis, differences in experimental setup like variable species and different (patient specific) material parameters were probable to have caused the differences in stress and strain results of the mechanical cardiac tests done by Dokos et al. [23] and Sommer et al. [24]. Therefore, when comparing the UMAT to experimental data different from the data for which the material parameters are optimised, it is likely that parts of the occuring errors are caused by differences in experimental setups. Nonetheless, the trends of the UMAT results and the experimental data were assumed to be similar, and therefore these were compared to each other.

	Dokos et al. [23]	Sommer et al. [24]	units
Specimen geometry	3x3x3	4x4x4	mm
Specimen species	porcine	human	-
Experiment temp.	4	37	deg
Loading speed	0.6 - 3	1	mm/min

Table 7.1: Differences in experimental setup may have caused the differences in stress and strain results of [23] and [24] in Fig. 6.9.

7.3 CONCLUSIONS AND FUTURE DIRECTIONS

This thesis has established a user subroutine UMAT that incorporates the combined HO and TVE material model. The user subroutine is designed to be used in personalised whole-heart FE-models. The passive- and active components can be optimised to personalise cardiac tissue properties to approximate both healthy and diseased hearts. Personalised components consist of patient-specific heart geometry, passive material properties and maximal active tension parameter and a scale factor providing the relation between the contraction in fibre- and sheet-direction. In the foreseen future the user subroutine may be included in a whole heart FE-model, in which the material model can be validated. Consecutively, this whole heart FE-model incorporating the proposed user subroutine can be combined with computational fluid dynamics resulting in a fluid-solid interaction model. Lastly, the aim of this thesis was to define a model representing the mechanical component of the cardiac functionality. In future, electric and chemical phenomena occurring in cardiac tissue, i.e. polarisation, excitation and propagation may be added.

The passive HO and active TVE model incorporated in the user subroutine UMAT, which is fully available in the supplementary material, will accommodate projects in need of an active material model, as well as provide for a starting point to develop a new UMAT. All in all, this thesis forms a significant step forward in the cardiac FE modelling field.

BIBLIOGRAPHY

[1] G. Savarese, P. M. Becher, L. H. Lund, P. Seferovic, G. M. C. Rosano, and A. J. S. Coats, "Global burden of heart failure: a comprehensive and updated review of epidemiology," *Cardiovascular Research*, 2022.

[2] S. S. Virani, A. Alonso, H. J. Aparicio, E. J. Benjamin, M. S. Bittencourt, C. W. Callaway, A. P. Carson, A. M. Chamberlain, S. Cheng, F. N. Delling, M. S. V. Elkind, K. R. Evenson, J. F. Ferguson, D. K. Gupta, S. S. Khan, B. M. Kissela, K. L. Knutson, C. D. Lee, T. T. Lewis, J. Liu, M. S. Loop, P. L. Lutsey, J. Ma, J. Mackey, S. S. Martin, D. B. Matchar, M. E. Mussolino, S. D. Navaneethan, A. M. Perak, G. A. Roth, Z. Samad, G. M. Satou, E. B. Schroeder, S. H. Shah, C. M. Shay, A. Stokes, L. B. Vanwagner, N.-Y. Wang, and C. W. Tsao, "Heart Disease and Stroke Statistics—2021 Update," *Circulation*, vol. 143, no. 8, 2021.

[3] H. Yu, P. J. Del Nido, T. Geva, C. Yang, A. Tang, Z. Wu, R. H. Rathod, X. Huang, K. L. Billiar, and D. Tang, "Patient-specific in vivo right ventricle material parameter estimation for patients with tetralogy of Fallot using MRI-based models with different zero-load diastole and systole morphologies," *International Journal of Cardiology*, vol. 276, pp. 93–99, 2019.

[4] B. Baillargeon, N. Rebelo, D. D. Fox, R. L. Taylor, and E. Kuhl, "The Living Heart Project: A robust and integrative simulator for human heart function," *European Journal of Mechanics - A/Solids*, vol. 48, pp. 38–47, 2014.

[5] H. Yu, P. J. del Nido, T. Geva, C. Yang, Z. Wu, R. H. Rathod, X. Huang, K. L. Billiar, and D. Tang, "A Novel Pulmonary Valve Replacement Surgery Strategy Using Contracting Band for Patients With Repaired Tetralogy of Fallot: An MRI-Based Multipatient Modeling Study," *Frontiers in Bioengineering and Biotechnology*, vol. 9, pp. 1–15, 2021.

[6] Dassault Systèmes Simulia Corp, "ABAQUS/STANDARD, version 2020," 2020.

[7] W. Sun, E. L. Chaikof, and M. E. Levenston, "Numerical Approximation of Tangent Moduli for Finite Element Implementations of Nonlinear Hyperelastic Material Models," *Journal of Biomechanical Engineering*, vol. 130, no. 6, p. 61003, 2008.

[8] G. A. Holzapfel and R. W. Ogden, "Constitutive modelling of passive myocardium: a structurally based framework for material characterization," *Philosophical Transactions of the Royal Society A: Mathematical, Physical and Engineering Sciences*, vol. 367, no. 1902, pp. 3445–3475, 2009.

[9] J. M. Guccione, L. K. Waldman, and A. D. McCulloch, "Mechanics of active contraction in cardiac muscle: Part II–Cylindrical models of the systolic left ventricle," *J Biomech Eng*, vol. 115, no. 1, pp. 82–90, 1993.

[10] E. Pierce, "Wikimedia Commons; Human Heart Anatomy, `https://commons.wikimedia.org/wiki/File:Diagram_of_the_human_heart_(cropped).svg`," 2022.

[11] W. F. Boron and E. L. Boulpaep, *Medical Physiology*. 2012.

[12] V. Sequeira and J. van der Velden, "Historical perspective on heart function: the Frank–Starling Law," dec 2015.

[13] L. M. Hanft, F. S. Korte, and K. S. Mcdonald, "Cardiac function and modulation of sarcomeric function by length," *Cardiovascular Research*, vol. 77, no. 4, pp. 627–636, 2007.

[14] R. E. Klabunde, "CV Physiology, https://www.cvphysiology.com/," 2022.

[15] T. F. Robinson, L. Cohen-Gould, S. M. Factor, M. Eghbali, and O. O. Blumenfeld, "Structure and function of connective tissue in cardiac muscle: collagen types I and III in endomysial struts and pericellular fibers.," *Scanning microscopy*, vol. 2, pp. 1005–1015, jun 1988.

[16] P. P. Purslow, "The Extracellular Matrix of Skeletal and Cardiac Muscle," in *Collagen*, pp. 325–357, Boston, MA: Springer, 2008.

[17] R. Avazmohammadi, J. S. Soares, D. S. Li, S. S. Raut, R. C. Gorman, and M. S. Sacks, "A Contemporary Look at Biomechanical Models of Myocardium," *Annual Review of Biomedical Engineering*, vol. 21, no. 1, pp. 417–442, 2019.

[18] S. De Jong, T. A. Van Veen, J. M. De Bakker, M. A. Vos, and H. V. Van Rijen, "Biomarkers of myocardial fibrosis," *Journal of Cardiovascular Pharmacology*, vol. 57, pp. 522–535, may 2011.

[19] F. C. Yin, C. C. Chan, and R. M. Judd, "Compressibility of perfused passive myocardium," *American Journal of Physiology-Heart and Circulatory Physiology*, vol. 271, no. 5, pp. H1864–H1870, 1996.

[20] B. M. Jackson, J. H. Gorman, S. L. Moainie, T. S. Guy, N. Narula, J. Narula, M. G. St. John-Sutton, L. H. Edmunds, and R. C. Gorman, "Extension of borderzone myocardium in postinfarction dilated cardiomyopathy," *Journal of the American College of Cardiology*, vol. 40, no. 6, pp. 1160–1167, 2002.

[21] R. Avazmohammadi, J. S. Soares, D. S. Li, T. Eperjesi, J. Pilla, R. C. Gorman, and M. S. Sacks, "On the in vivo systolic compressibility of left ventricular free wall myocardium in the normal and infarcted heart," *Journal of Biomechanics*, vol. 107, p. 109767, 2020.

[22] H. Liu, J. S. Soares, J. Walmsley, D. S. Li, S. Raut, R. Avazmohammadi, P. Iaizzo, M. Palmer, J. H. Gorman, R. C. Gorman, and M. S. Sacks, "The impact of myocardial compressibility on organ-level simulations of the normal and infarcted heart," *Nature*, vol. 11, no. 1, 2021.

[23] S. Dokos, B. H. Smaill, A. A. Young, and I. J. LeGrice, "Shear properties of passive ventricular myocardium," *Am J Physiol Heart Circ Physiol*, vol. 283, no. 6, pp. H2650–9, 2002.

[24] G. Sommer, A. J. Schriefl, M. Andrä, M. Sacherer, C. Viertler, H. Wolinski, and G. A. Holzapfel, "Biomechanical properties and microstructure of human ventricular myocardium," *Acta Biomater*, vol. 24, pp. 172–192, 2015.

[25] G. M. Fomovsky, S. Thomopoulos, and J. W. Holmes, "Contribution of extracellular matrix to the mechanical properties of the heart," *Journal of Molecular and Cellular Cardiology*, vol. 48, pp. 490–496, mar 2010.

[26] Z. Wang, M. J. Golob, and N. C. Chesler, "Viscoelastic Properties of Cardiovascular Tissues," *Viscoelastic and Viscoplastic Materials*, sep 2016.

[27] F. Barış, C. Cansız, H. Dal, M. Kaliske, F. Barışçan, and B. Cansız, "An orthotropic viscoelastic material model for passive myocardium: theory and algorithmic treatment," *Computer Methods in Biomechanics and Biomedical Engineering*, vol. 18, pp. 1160–1172, aug 2015.

[28] O. Gültekin, G. Sommer, and G. A. Holzapfel, "An orthotropic viscoelastic model for the passive myocardium: continuum basis and numerical treatment," *Computer Methods in Biomechanics and Biomedical Engineering*, vol. 19, pp. 1647–1664, nov 2016.

[29] E. Marieb and K. Hoehn, *Anatomy Physiology*. Pearson Education, 4th editio ed., 2011.

[30] Rice University, "Anatomy Physiology, https://courses.lumenlearning.com/suny-ap1/chapter/muscle-fiber-contraction-and-relaxation/," 2022.

[31] L. J. Dupuis, J. Lumens, T. Arts, and T. Delhaas, "Mechano-chemical Interactions in Cardiac Sarcomere Contraction: A Computational Modeling Study," *PLOS Computational Biology*, vol. 12, no. 10, p. e1005126, 2016.

[32] K. L. Sack, B. Baillargeon, G. Acevedo-Bolton, M. Genet, N. Rebelo, E. Kuhl, L. Klein, G. M. Weiselthaler, D. Burkhoff, T. Franz, and J. M. Guccione, "Partial LVAD Restores Ventricular Outputs and Normalizes LV but not RV Stress Distributions in the Acutely Failing Heart in Silico," *The International Journal of Artificial Organs*, vol. 39, no. 8, pp. 421–430, 2016.

[33] R. M. Fuchs, J. A. Brinker, W. Maughan, M. L. Weisfeldt, and F. C. P. Yin, "Coronary flow limitation during the development of ischemia," *The American Journal of Cardiology*, vol. 48, no. 6, pp. 1029–1036, 1981.

[34] J. M. Guccione, A. D. McCulloch, and L. K. Waldman, "Passive material properties of intact ventricular myocardium determined from a cylindrical model," *J Biomech Eng*, vol. 113, no. 1, pp. 42–55, 1991.

[35] J. D. Humphrey and F. C. Yin, "On constitutive relations and finite deformations of passive cardiac tissue: I. A pseudostrain-energy function," *J Biomech Eng*, vol. 109, no. 4, pp. 298–304, 1987.

[36] J. D. Humphrey, R. K. Strumpf, and F. C. Yin, "Determination of a constitutive relation for passive myocardium: I. A new functional form," *J Biomech Eng*, vol. 112, no. 3, pp. 333–339, 1990.

[37] K. D. Costa, P. J. Hunter, J. M. Rogers, J. M. Guccione, L. K. Waldman, and A. D. McCulloch, "A three-dimensional finite element method for large elastic deformations of ventricular myocardium: I–Cylindrical and spherical polar coordinates," *J Biomech Eng*, vol. 118, no. 4, pp. 452–463, 1996.

[38] I. J. LeGrice, B. H. Smaill, L. Z. Chai, S. G. Edgar, J. B. Gavin, and P. J. Hunter, "Laminar structure of the heart: ventricular myocyte arrangement and connective tissue architecture in the dog," *Am J Physiol*, vol. 269, no. 2 Pt 2, pp. H571–82, 1995.

[39] P. J. Hunter, A. D. McCulloch, and H. E. Ter Keurs, "Modelling the mechanical properties of cardiac muscle," *Prog Biophys Mol Biol*, vol. 69, no. 2-3, pp. 289–331, 1998.

[40] K. D. Costa, J. W. Holmes, and A. D. McCulloch, "Modelling cardiac mechanical properties in three dimensions," *Philosophical Transactions of the Royal Society of London. Series A: Mathematical, Physical and Engineering Sciences*, vol. 359, no. 1783, pp. 1233–1250, 2001.

[41] H. Schmid, M. P. Nash, A. A. Young, and P. J. Hunter, "Myocardial material parameter estimation-a comparative study for simple shear," *J Biomech Eng*, vol. 128, no. 5, pp. 742–750, 2006.

[42] K. L. Sack, E. Aliotta, D. B. Ennis, J. S. Choy, G. S. Kassab, J. M. Guccione, and T. Franz, "Construction and Validation of Subject-Specific Biventricular Finite-Element Models of Healthy and Failing Swine Hearts From High-Resolution DT-MRI," *Frontiers in Physiology*, vol. 9, 2018.

[43] G. A. Holzapfel, *Nonlinear solid mechanics: a continuum approach for engineering science*. 2000.

[44] H. Wijkstra and H. B. K. Boom, "Left-ventricular dynamic model based on constant ejection flow periods," *IEEE Transactions on Biomedical Engineering*, vol. 38, no. 12, pp. 1204–1212, 1991.

[45] H. E. Ter Keurs, W. H. Rijnsburger, R. Van Heuningen, and M. J. Nagelsmit, "Tension development and sarcomere length in rat cardiac trabeculae. Evidence of length-dependent activation," *Circulation Research*, vol. 46, no. 5, pp. 703–714, 1980.

[46] H. E. Ter Keurs, W. H. Rijnsburger, and R. van Heuningen, "Restoring forces and relaxation of rat cardiac muscle," *European Heart Journal*, vol. 1, pp. 67–80, jan 1980.

[47] R. Van Heuningen, W. H. Rijnsburger, and H. E. Ter Keurs, "Sarcomere length control in striated muscle," *https://doi.org/10.1152/ajpheart.1982.242.3.H411*, vol. 11, no. 3, 1982.

[48] M. Daniels, M. I. Noble, H. E. Ter Keurs, and B. Wohlfart, "Velocity of sarcomere shortening in rat cardiac muscle: relationship to force, sarcomere length, calcium and time.," *The Journal of Physiology*, vol. 355, pp. 367–381, oct 1984.

[49] H. Ter Keurs, P. De Tombe, P. Backx, and T. Iwazumi, "The effects of sarcomere length and Ca++ on force and velocity of shortening in cardiac muscle.," *Adv Exp Med Biol.*, vol. 226, pp. 581–93, 1988.

[50] J. W. Krueger, K. Tsujioka, T. Okada, C. S. Peskin, and H. M. Lacker, "A "give" in tension and sarcomere dynamics in cardiac muscle relaxation.," *Advances in experimental medicine and biology*, vol. 226, pp. 567–580, 1988.

[51] D. R. Nolan, A. L. Gower, M. Destrade, R. W. Ogden, and J. P. McGarry, "A robust anisotropic hyperelastic formulation for the modelling of soft tissue," *Journal of the Mechanical Behavior of Biomedical Materials*, vol. 39, pp. 48–60, 2014.

[52] D. R. Nolan, C. Lally, and J. P. McGarry, "Understanding the deformation gradient in Abaqus and key guidelines for anisotropic hyperelastic user material subroutines (UMATs)," *Journal of the Mechanical Behavior of Biomedical Materials*, vol. 126, pp. 1–48, 2019.

[53] ABQ 2020 Documentation, "Abaqus 2020 Documentation: UMAT, `https://help.3ds.com/2020/english/dssimulia_established/simacaesubrefmap/simasub-c-umat.htm?contextscope=all`," 2020.

[54] V. Prot and B. Skallerud, "Nonlinear solid finite element analysis of mitral valves with heterogeneous leaflet layers," *Computational Mechanics*, vol. 43, no. 3, pp. 353–368, 2009.

[55] ABQ 2020 Documentation, "Abaqus 2020 Documentation: Anisotropic Hyperelastic Material Behavior, `https://help.3ds.com/2021/english/dssimulia_established/simacaetherefmap/simathe-c-anisohyperelastic.htm?contextscope=all`," 2020.

[56] H. Liu and W. Sun, "Computational efficiency of numerical approximations of tangent moduli for finite element implementation of a fiber-reinforced hyperelastic material model," *Computer Methods in Biomechanics and Biomedical Engineering*, vol. 19, no. 11, pp. 1171–1180, 2016.

[57] G. A. Ateshian and K. D. Costa, "A frame-invariant formulation of Fung elasticity," *Journal of Biomechanics*, vol. 42, no. 6, pp. 781–785, 2009.

[58] ABQ 2020 Documentation, "Abaqus 2020 Documentation: Stress Rates, https://help.3ds.com/2020/english/dssimulia_established/simacaetherefmap/simathe-c-stressrates.htm?contextscope=all," 2020.

[59] H. Liu and W. Sun, "Numerical Approximation of Elasticity Tensor Associated With Green-Naghdi Rate," *Journal of Biomechanical Engineering*, vol. 139, no. 8, 2017.

[60] ABQ 2020 Documentation, "Abaqus 2020 Documentation: Conventions https://help.3ds.com/2020/english/dssimulia_established/simacaemodrefmap/simamod-c-conventions.htm?contextscope=all," 2020.

[61] H. Fehervary, L. Maes, J. Vastmans, G. Kloosterman, and N. Famaey, "How to implement user-defined fiber-reinforced hyperelastic materials in finite element software," *Journal of the Mechanical Behavior of Biomedical Materials*, vol. 110, p. 103737, 2020.

[62] M. Holland, "The Hitchhiker's Guide To Abaqus, https://github.com/mholla/hitchhikers-guide-to-abaqus," 2012.

[63] F. Marin, *Development of an MRI-based finite element cardiac model for repaired Tetralogy of Fallot biomechanical characterization*. PhD thesis, Erasmus MC, 2019.

[64] I. The MathWorks, "MATLAB R2019b," 2019.

[65] M. Peirlinck, *Bridging spatiotemporal scales in biomechanical models for living tissues : from the contracting Esophagus to cardiac growth*. PhD thesis, UGent, 2019.

[66] E. H. Sonnenblick, "Series elastic and contractile elements in heart muscle: changes in muscle length," *American Journal of Physiology-Legacy Content*, vol. 207, no. 6, pp. 1330–1338, 1964.

[67] W. W. Parmley, L. Chuck, C. Kivowitz, J. M. Matloff, and H. J. Swan, "In vitro length-tension relations of human ventricular aneurysms. Relation of stiffness to mechanical disadvantage," *Am J Cardiol*, vol. 32, no. 7, pp. 889–894, 1973.

[68] L. L. Demer and F. C. Yin, "Passive biaxial mechanical properties of isolated canine myocardium," *The Journal of Physiology*, vol. 339, no. 1, pp. 615–630, 1983.

[69] F. C. P. Yin, R. K. Strumpf, P. H. Chew, and S. L. Zeger, "Quantification of the mechanical properties of noncontracting canine myocardium under simultaneous biaxial loading," *Journal of Biomechanics*, vol. 20, no. 6, pp. 577–589, 1987.

[70] V. P. Novak, F. C. P. Yin, and J. D. Humphrey, "Regional mechanical properties of passive myocardium," *Journal of Biomechanics*, vol. 27, no. 4, pp. 403–412, 1994.

[71] B. Smaill and P. Hunter, "Structure and Function of the Diastolic Heart: Material Properties of Passive Myocardium," in *Theory Of Heart*, pp. 1–29, Springer New York, 1991.

[72] C. Holubarsch, "Shortening versus isometric contractions in isolated human failing and non-failing left ventricular myocardium: dependency of external work and force on muscle length, heart rate and inotropic stimulation," *Cardiovascular Research*, vol. 37, no. 1, pp. 46–57, 1998.

[73] ABQ 2020 Documentation, "Abaqus 2020 Documentation: Anisotropic hyperelastic behavior, https://help.3ds.com/2020/english/dssimulia_established/simacaematrefmap/simamat-c-anisohyperelastic.htm?contextscope=all," 2020.

[74] M. Tigchelaar, *Focus, AAN/UIT*. 1 ed., 2019.

A | APPENDICES

APPENDIX: SUPPLEMENTARY MATERIAL

The material supplementary to this thesis is available on request by contacting `mplab-3me@tudelft.nl` and `a.c.akyildiz@tudelft.nl`.

APPENDIX: TENSOR PRODUCTS

In this thesis the following definitions of tensor products are used, defined by [43].

Double dot product: For two second-order tensors $\mathbf{A}$ and $\mathbf{B}$, the result is a scalar.

$$\mathbf{A} : \mathbf{B} = A_{ij}B_{ij} \tag{A.1}$$

For two fourth-order tensors $\mathbb{A}$ and $\mathbb{B}$, the result is a second order tensor.

$$(\mathbb{A} : \mathbb{B})_{ijkl} = A_{ijmn}B_{mnkl} \tag{A.2}$$

For a fourth-order tensors $\mathbb{A}$ and a second order tensor $\mathbf{C}$, the result is a second order tensor.

$$(\mathbb{A} : \mathbf{C})_{ij} = A_{ijkl}C_{kl} \tag{A.3}$$

Dyadic products: For two second-order tensors $\mathbf{A}$ and $\mathbf{B}$

$$(\mathbf{A} \otimes \mathbf{B})_{ijkl} = A_{ij}B_{kl} \tag{A.4}$$

$$= \begin{bmatrix} A_{1,1} \cdot \mathbf{B} & '' & A_{1,2} \cdot \mathbf{B} & '' \\ '' & '' & '' & '' \\ A_{2,1} \cdot \mathbf{B} & '' & A_{2,2} \cdot \mathbf{B} & '' \\ '' & '' & '' & '' \end{bmatrix} \tag{A.5}$$

$$(\mathbf{A} \underline{\otimes} \mathbf{B})_{ijkl} = A_{ik}B_{jl} \tag{A.6}$$

$$= \begin{bmatrix} \mathbf{A} \cdot B_{1,1} & '' & \mathbf{A} \cdot B_{1,2} & '' \\ '' & '' & '' & '' \\ \mathbf{A} \cdot B_{2,1} & '' & \mathbf{A} \cdot B_{2,2} & '' \\ '' & '' & '' & '' \end{bmatrix} \tag{A.7}$$

$$(\mathbf{A} \odot \mathbf{B})_{ijkl} = (\mathbf{A} \overline{\otimes} \mathbf{B})_{ijkl}$$
$$= \frac{1}{2}(A_{ik}B_{jl} + A_{il}B_{jk}) = \frac{1}{2}(\mathbf{A} \underline{\otimes} \mathbf{B} + \mathbf{A} \otimes \mathbf{B}) \tag{A.8}$$

Therefore, the tensor product $\mathbf{C}^{-1}$ is defined as below.

$$-(\mathbf{C}^{-1} \odot \mathbf{C}^{-1})_{ijkl} = -\frac{1}{2}(C_{ik}^{-1}C_{jl}^{-1} + C_{il}^{-1}C_{jk}^{-1}) = \frac{\partial C_{ij}^{-1}}{\partial C_{kl}^{-1}} \tag{A.9}$$

APPENDIX: DERIVATIVES OF THE HOLZAPFEL–OGDEN STRAIN ENERGY FUNCTION WRITTEN OUT

The first derivatives of the HO SEF with relation to the invariants can be written out as follows

$$\psi_1 = \frac{\partial \Psi}{\partial \bar{I}_1} = \frac{a}{2}\exp[b(\bar{I}_1 - 3)], \tag{A.10}$$

$$\psi_{4f} = \frac{\partial \Psi}{\partial \bar{I}_{4f}} = a_f(\bar{I}_{4f} - 1)\exp[b_f(\bar{I}_{4f} - 1)^2], \tag{A.11}$$

$$\psi_{4s} = \frac{\partial \Psi}{\partial \bar{I}_{4s}} = a_s(\bar{I}_{4s} - 1)\exp[b_s(\bar{I}_{4s} - 1)^2], \tag{A.12}$$

$$\psi_{8fs} = \frac{\partial \Psi}{\partial \bar{I}_8} = a_{fs}(\bar{I}_{8fs})\exp[b_{fs}(\bar{I}_{8fs})^2]. \tag{A.13}$$

Similarly, the second derivatives of the HO SEF with relation to the invariants can be written as follows

$$\psi_1^{''} = \frac{\partial^2 \Psi}{(\partial \bar{I}_1)^2} = \frac{ab}{2}\exp[b(\bar{I}_1 - 3)]), \tag{A.14}$$

$$\psi_{4f}^{''} = \frac{\partial^2 \Psi}{(\partial \bar{I}_{4f})^2} = (a_f\exp[b_f(\bar{I}_{4f} - 1)^2])(2b_f(\bar{I}_{4f} - 1)^2 + 1), \tag{A.15}$$

$$\psi_{4s}^{''} = \frac{\partial^2 \Psi}{(\partial \bar{I}_{4s})^2} = (a_s\exp[b_s(\bar{I}_{4s} - 1)^2])(2b_s(\bar{I}_{4s} - 1)^2 + 1), \tag{A.16}$$

$$\psi_{8fs}^{''} = \frac{\partial^2 \Psi}{(\partial \bar{I}_{8fs})^2} = (a_{fs}\exp[b_{fs}(\bar{I}_{8fs})^2])(2b_{fs}(\bar{I}_{8fs})^2 + 1). \tag{A.17}$$

B | POSTFACE

Reflection

Looking back at the beginning of this thesis project, Covid had spread over the world more than half a year. The 'thuiswerkadvies' (working at home advice) from Prime Minister Mark Rutte was applicable for everyone in the Netherlands. I just finished the first year of my master. Due to the course Computational Mechanics of Tissues and Cells that sparked my interest, the choice for this project about modelling hearts was quickly made.

Most of this thesis is produced in my student-room in Rotterdam. Working from home had its challenges, as collaborating and asking for help had a higher threshold, causing the amount of trial-and-error work to increase significantly. On the other hand, it has given me a boost in my personal development and the sense of responsibility for this. As knowledge worker, I believe that focus is one of the most important tools you have. Reading about this brought me to clichés like 'aanraken is afmaken' [74], which became my device for periods of time, learning healthy working habits. Working on my thesis during Covid has increased my ability of working independently and improved my problem-solving skills.

Now, close to the end of my master thesis, a lot has changed. My knowledge of continuum mechanics and ability to work with Abaqus and Matlab, and programming languages Python and Fortran have increased greatly. Also, we are slowly going back to the 'old normal', going to the EMC again for the majority of the week, and getting to know everyone in the department in person.

Acknowledgements

My master end project as well as the personal learning curve that I went through were not possible without Ali, my supervisor, whom I would like to thank for the insights I experienced during our discussions, and giving me trust and time to grow within the project. I also want to thank Mathias Peirlinck for your knowledge and advice which often came on just the right moment. I am grateful for Savine Minderhoud, for initiating this project and answering all my clinical related questions. I would like to thank all my coworkers at the Biomedical Engineering and Cardiology Department of the Erasmus MC, for joining me for lunches outside in the sun and hangboard competitions! Lastly, I want to thank my dad for reading my thesis and insightful discussions about science in general.

According to Tigchelaar [74], zooming out now and then is essential for the brain in order to fully focus later, time where the brain 'does mainly nothing' (DMN). To this end I want to thank my friends and family for their support and the needed DMN-time outside working hours. Especially Loes and Hector, for welcoming me at your home for the last 2 months of my thesis. Also, the rest of the dalmutties, Marta, Marlene, Yenthe, for emotional support and coaching. My climbing buddies, for training with me and going on weekends outside. Last but not least, thank you Menno for being so patient, I will join you in France soon!